Low Temperature Epitaxial Growths of III-Nitride Semiconductors on ITO Glass Substrates

Jonny Tot

Presented to the faculty of Electrical and Computer Engineering in partial fulfillment for a M.Sc. degree

Lakehead University

Thunder Bay, Ontario

April 2016

Table of Contents

List of Figures

List of acronyms

Light emitting diode (LED)

High Electron Mobility Transistor (HEMT)

Quantum Well (QW)

External Quantum Efficiency (EQE)

Indium Tin Oxide (ITO)

Transparent Conductive Oxide (TCO)

Face Centered Cubic (FCC)

Thermal Coeffcient of Expansion (TCE)

Root Mean Square (RMS)

Hydride Vapour Phase Epitaxy (HVPE)

Chemical Vapour Deposition (CVD)

Atomic Layer Deposition (ALD)

Molecular Beam Epitaxy (MBE)

Ultra-High Vacuum (UHV)

Field Effect Transistor (FET)

Reflection high-energy electron diffraction (RHEED)

Metal-Organic Chemical Vapour Deposition (CVD)

Radio Frequency (RF)

Remote Plasma (RP)

Atomic Force Microscope (AFM)

X-ray Diffraction (XRD)

Scanning Electron Microscope (SEM)

Energy Dispersive X-ray Analysis (EDX)

Ultraviolet (UV)

Infrared (IR)

Residual Gas Analyzer (RGA)

Full Width at Half Maximum (FWHM)

Chapter 1: Introduction

1.1 Summary of work

Chapter 1 serves as an introduction to the electronic, optical and physical properties of the nitride material system that have made it a heavily researched group of semiconductors. The need for heteroepitaxy and various commercially successful substrates will be discussed along with the motivation of this thesis. Some general history will be provided as well as the challenges faced by these materials in commercialization. Chapter 2 will focus on current and past growth techniques used for nitrides, outlining how epitaxy occurs in these systems with their respective benefits and faults. Chapter 3 will give an overview on the characterization tools used throughout this research. An understanding of how these tools operate will assist in interpreting data correctly. Combined with knowledge from chapter 2 it may also give insight on what needs to change about growth conditions to optimize growth. Chapter 4 will present the growth results from various characterization tools discussed in chapter 3. Conclusions about the data from each material system will be discussed. Chapter 5 will focus on theoretical calculations for InN. Initial results for InN show it to be the most promising material. A theoretical analysis of common impurities on the electronic band structure of InN will help in interpreting optical properties of the material. The central research contributions of the author in this thesis can be summarized as the development of III-Nitrides growth recipes for each material, characterization of the results, and the application of LCAO theory to the InN system for common impurities found in the growth technique examined.

1.2 Overview

The group III-nitride family of semiconductors has been an important area of research since the demonstration of high quality p-type GaN for LEDs in the early 90's. The family of materials includes InN, AlN and GaN, wherein they all share a common crystal structure and a range of properties that can be engineered through alloying. Perhaps one of the most important properties that can be tailored is the band gap, which maintains a direct type through all compositions. This is important because the range of band gaps covered by the materials system begins with 0.69eV at InN [1] and varies continuously to AlN at 6.026 - 6.28eV and GaN in the middle with 3.42eV [2]. A simple weighted fraction can be used to approximate the band gap and lattice constant of ternary alloys. A plot of band gap vs. lattice constant can be seen in fig. 1

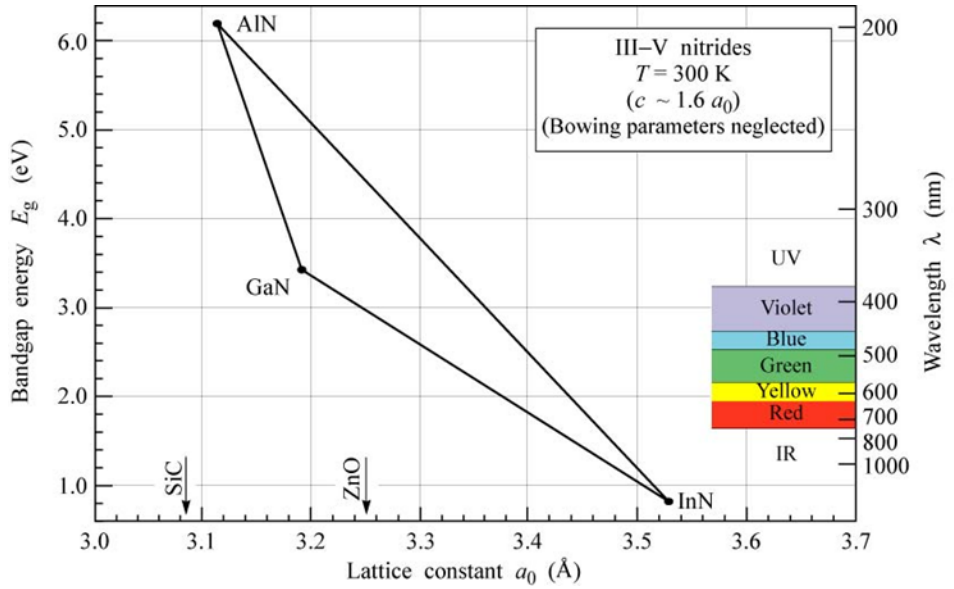

showing a linear interpolation of alloy parameters.

Figure 1: Plot of band gap vs lattice constant for nitride semiconductors with a linear interpolation between them [3].

The wide variability of the direct band gap led to the earliest commercially successful device using the nitride materials, the blue LED. The utility of a continuous direct band gap over such a range is however not limited to LEDs, it is invaluable for photovoltaics and optoelectronic sensor devices. Since the development of the blue LED other commercially successful devices based on these materials have emerged, including short-wavelength laser diodes, high density optical storage mediums and display technologies.

The family of materials also exhibits remarkable electrical and physical properties. Aluminum and gallium containing materials exhibit breakdown fields of $1.2–1.8x10^6$ and $3–5x10^6$ V/cm respectively, upwards of an order of magnitude higher than silicon [2]. Predictions of low field mobility limits for electrons in GaN and InN at 300K are as high as 1400 [2] and 14000 [4] $cm^2V^{-1}s^{-1}$ respectively, with critical fields of 45, 140 and 450 kV/cm for InN, GaN and AlN [5]. These electrical properties translate into a large incentive for developing high power and high frequency devices where silicon and alternatives cannot operate. The thermal conductivity of GaN (2.3 W/cm K^{-1}) and AlN (3.2 W/cm K^{-1}) [2] are also superior to silicon (1.3 W/cm K^{-1}) [6], giving them a greater ability to dissipate heat in high power devices. GaN and AlN also exhibit extremely high melting points and a resistance to ionizing radiation, making them suitable for harsh environments such as space [2].

In addition to robust physical and electrical properties the nitride family also exhibits unique as piezo and pyro electric properties not commonly found in other material systems. These properties arise from asymmetries in the wurtzite crystal structure, which is the most thermodynamically stable phase for all of the nitrides. Though wurtzite is most commonly found in literature for device research, cubic structures exists as a metastable phase and can be intentionally created through deposition on cubic substrates. The only structural difference

between the two phase is the wurtzite stacking order is AaBbAaBb along the [0001] direction and cubic is AaBbCcAaBbCc along the [111] direction. A rock salt phase has also been reported, but is only stable under extremely high pressures [2].

The main difference between the wurtzite and cubic phase is the stacking order of metal and N atoms and a lack of symmetry in the case of wurtzite along the c-axis. The lack of symmetry for wurtzite creates a significant polarization within the crystal which is the source of piezoelectric and spontaneous polarization induced charge effects. These effects can be exploited for devices, but require special attention for design.

The convention of polarity direction is to point from the metal anion species to the nitrogen cation. The magnitude of the polarization varies between materials with GaN, AlN and InN having values of of -0.029 C/m^2, -0.081 C/m^2 and -0.032 C/m^2 for respectively [7]. The presence of this polarization has led to two distinct growth types, where the polarization vector at the surface either points towards to substrate or away from it, assuming the growth direction is along the c-axis. This is significant as change of polarization vectors causes charge accumulation at heterointerfaces. Initial surface conditions and growth conditions can be varied to control the direction of the polarization vector. The presence of these carriers can be beneficial in certain devices, such as the HEMT, but may prove detrimental to other structures, such as quantum wells in LEDs, where the induced fields in quantum well structures spatially separates minority carriers, leading to a reduction in external quantum efficiency in QW devices. Growth along a non-polar axis is an active area of research for this reason. An illustration of the behavior of the polarization vector magnitude for InGaN at different orientations can be seen in fig. 2.

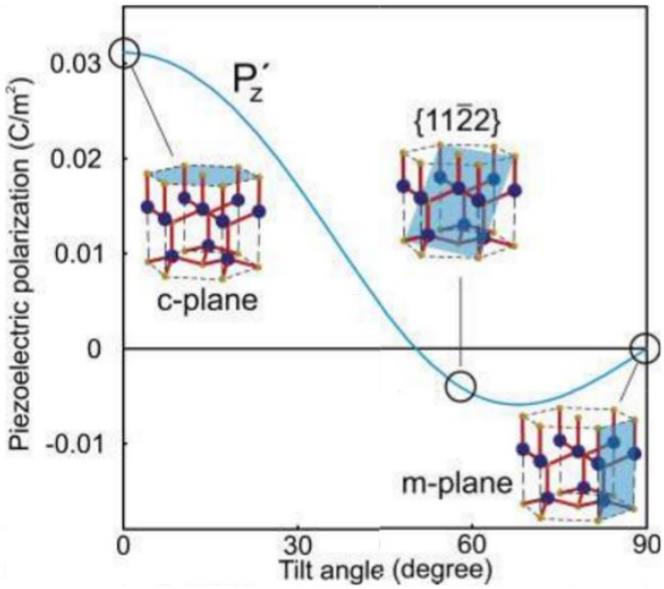

Figure 2: Polarization magnitude in InGaN compounds at various tilt angles [8].

1.3 Motivation

While the physical properties of these materials makes them good candidates for displacing current Si and GaAs technology, the distinct disadvantages of these materials are difficulty p-type doping, difficultly synthesizing high indium content alloys and the lack of bulk substrate production.

P-type doping in nitride semiconductors has been accomplished using Zn, Be and Mg donor dopants [9] [10]. Of these three, Mg has proven to most successful because it has the lowest ionization energy of approximately 200meV. This is still a relatively significant amount of energy and at room temperature it can be expected that less than 1% of incorporated dopants are activated. In addition to this, magnesium is also known to form independent structures within the nitride lattice at high concentrations and can form neutral Mg-H complexes with hydrogen contamination [11].

High indium content alloys have proven difficult to synthesize due to the effects of spinodal decomposition [12] and non-radiative native defects [13]. This has led to difficulties in production of emission devices in the green-yellow part of the spectrum. Fig. 3 shows a plot of EQE in LED devices as a function of wavelength overlaid on plot of luminous eye response.

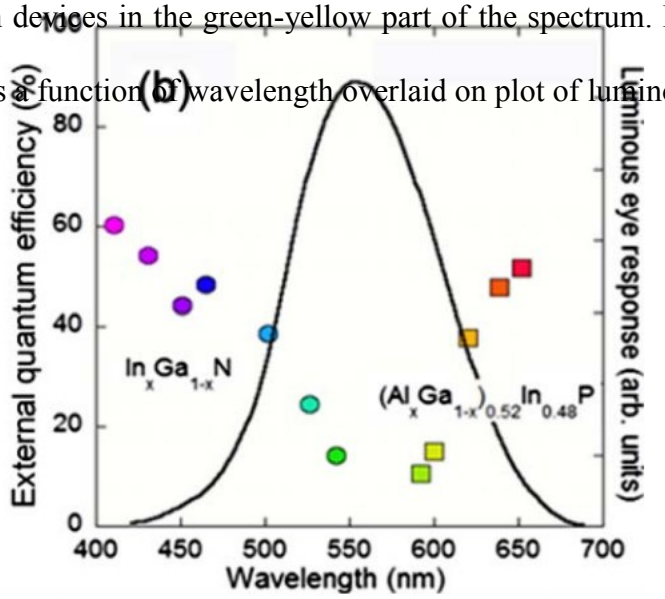

Figure 3: Demonstration of EQE drop as indium incorporation increases in LEDs [8].

It is clear that the green-yellow part of the spectrum, which relies on high indium content alloys, suffers efficiency losses. Unfortunately this is also the most sensitive part of the spectrum for eye response, which has led to white light sources relying on phosphorescence techniques and relatively high red and blue contents.

The deteriorating effects in indium nitride occur at relativly low temperatures compared to the growth conditions for AlN and GaN by conventinal MOCVD and MBE utilizing ammonia as a nitrogen precursor. Because of this, InN growth has typically been done around 500°C [14]. By extention of improving InN quality, the growth of important ternary compounds such as containing InAlN and InGaN at low temperature are benefitted.

Currently the largest commercially successful substrate is silicon. Deposition at low temperatures can prove beneficial for silicon technology but also allows for growth on novel substrates such as glass, where high thermal expansion for low cost soda lime) coefficients and/or low melting points prohibit high temperature growth. Ultimately the goal of this thesis is to establish the feasibility of low temperature deposition of III-Nitrides on glass substrates utilizing the unique reactor technology at Lakehead University. This novel low temperature deposition will address the issues of limited substrate diameter and can be possibly be extended to other amorphous substrates. In addition to growth results, some calculations will be performed using linear combination of atomic orbitals for the analysis of the effects of non-stoichiometric incorporation of nitrogen in the lattice of InN, carbon incorporation, and interstitial oxygen contaminants. InN was chosen as the focus of these calculations because of preliminary results showing the most promise with InN.

1.4 Crystal Properties

1.4.1 Wurtzite

All III-nitride semiconductors and their alloys share a common wurtzite crystal as their lowest energy phase. The structure can be described as two interpenetrating hexagonal close packed structures with a translation along the c-axis of 5/8 of its lattice constant c_0. The unit cell formed can be seen in fig. 4 along with the physical dimensions of each material.

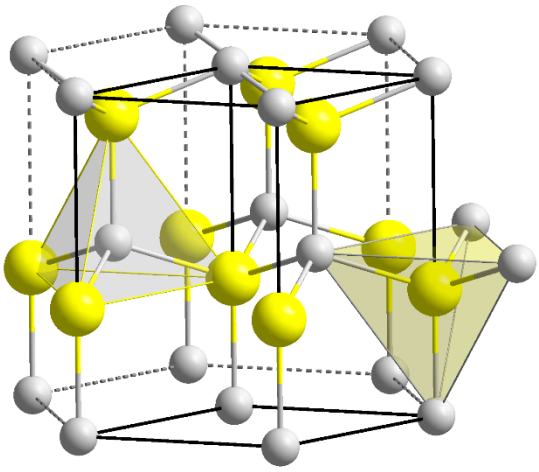

Material	AlN	GaN	InN
a_0 (Å)	3.112	3.189	3.54
c_0 (Å)	4.982	5.185	5.705
c_0/a_0	1.601	1.627	1.612
u	0.380	0.376	0.377

Figure 4: Unit cell of III-Nitride semiconductors along with dimensional properties. The radial and axial lattice parameters are a0 and c0 respectively and u is the interatomic distance parameter [2], [15].

1.4.2 Indium Oxide

Tin doped indium oxide (ITO) is a well known transparent conducting oxide (TCO) material that has been historically used a front side contact for optoelectronic and photovoltaic devices. In contact applications ITO is typically deposited as amorphous and low temperature thermal treatments are performed. The advantage of this is low temperature deposition methods and substrates, smoother surfaces, large area deposition and isotropic etching properties [16], [17]. Indium oxide begins to thermally anneal as low as 75°C into its thermodynamically stable bixbyite structure with the (111) surface being the lowest energy surface plane [17]. The bixbyite structure resembles a simpler FCC structure, but one quarter of anion sites are vacant. The vacancies result in corner, edge and face sharing distortions of the FCC unit cell and a variation

of In-In bond lengths from 3.34Å at edge sharing sites and 3.83Å at corner sharing sites [17]. Fig. 5 shows the result of this vacancy on varies surfaces of the unit cell.

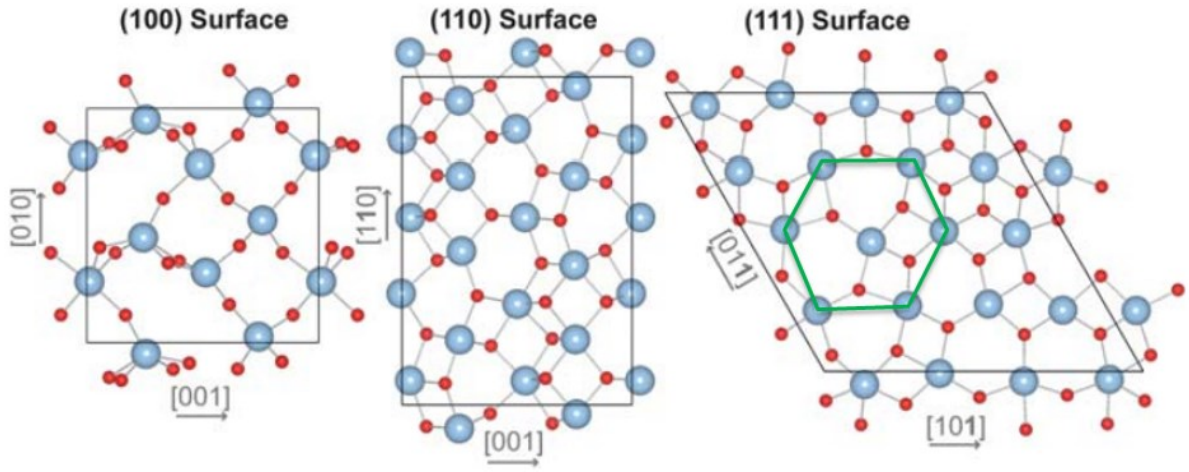

Figure 5: Surfaces of various indium oxide planes. The (111) surface has a face similar to cubic structures such as silicon, but is slightly distorted, leading to variations in bond length [17].

From the physical spacing of indium atoms on the (111) surface of indium oxide it can be expected that deposition of indium nitride will have the lowest lattice mismatch, as the spacing of indium atoms on the c-plane are close to the average spacing of In atoms on the (111) face of InO. The resulting lattice mismatch with GaN is similar in magnitude to silicon in the worst case. Because of the physical arrangement of the indium atoms, the (111) and parallel planes should provide the highest quality deposition surfaces for nitrides on glass.

1.5 Heteroepitaxy

Modern crystal growth techniques are the cornerstone of the electronics industry. The development of high quality crystal growth and complex characterization systems has largely been fueled for the development of this industry. Through decades of characterization and optimization of various growth processes, most bulk growth processes for the semiconductor

industry have relied on liquid melt techniques. The most common process used is the Czochralski method. In this method a seed crystal is lowered into a liquid melt of the desired material and slowly rotated and lifted from the melt. The result is a large boule of the material with the same structure as the seed. Liquid melt methods are valuable for large scale production.

1.6 Substrates

The choice of a substrate for nitride epitaxy comes with a trade-off of differing levels of mismatch and cost. An overview of substrate features can be seen in table 1. Further details of each substrate are outlined in proceeding sections.

Table 1: Properties of GaN and substrate materials.

	Sapphire	SiC	Si	GaN	ITO Glass
Lattice Mismatch (%)	16	3.5	17	-	4.8 – 17 (ITO)
TCE Mismatch (%)	-30	20	53	-	-48 (Glass) -30 (ITO)
Thermal conductivity (W/cm-K)	0.4	3.0-3.8	1.5	2.3	0.9 (Glass) 0.4 (ITO)
Wafer Diameter (mm)	200	150	400	50	-
Cost	High	Very High	Low	Very High	Low

1.6.1 Sapphire

Sapphire was the first substrate used by Amano et al. in 1986 and was the substrate used in the first commercially successful devices [18]. It has a rhombohedral lattice with a radial lattice constant of 4.759Å [19]. Investigation of the epitaxial relationship between sapphire substrates and wurtzite overlayers has shown that the overlayers experience a 30 degree in plane rotation to align the layers such that the epitaxial relationship is $[0001]_{III\text{-}N}||[0001]_{sap}$ and $[10\underline{1}0]_{III\text{-}N}||[11\underline{2}0]_{sap}$ [20]. A sample calculation and illustration for GaN can be seen in fig. 6.

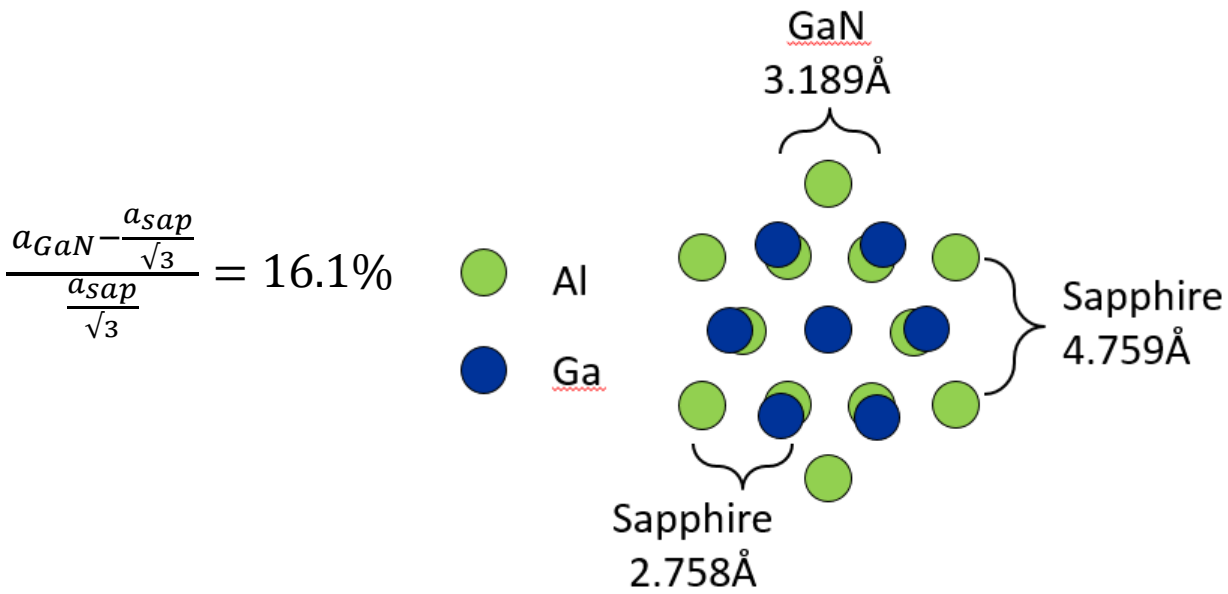

Figure 6: epitaxial relationship and lattice mismatch of sapphire with GaN.

Of all the commercially successful substrates, sapphire is the highest electrically insulating ($\rho = 1x10^{14}$ Ω-cm at 293K) and has the lowest thermal conductance (0.4 W/cm 293K) [19]. These properties are undesirable for devices, leading to poor dissipation of heat from junctions and a requirement for front side contacts to devices. Sapphire is however cheaper than

bulk SiC wafers, offers lower lattice mismatch than silicon and is extremely stable. It is also important to note that sapphire has a high TCE [19] compared to GaN (5.59×10^{-6} K^{-1} [2]) and exerts a compressive force on cooling. High compressive forces do not produce cracks in materials, but significant amounts may produce defects and bowing of the wafer.

1.6.2 Silicon Carbide

6H-SiC is one of many polytypes of silicon carbide and along with 4H-SiC and 3C-SiC is one of the most commonly used for electronics. 6H-SiC has a hexagonal lattice structure similar to III-Nitrides and when epitaxially deposited, their lattice planes are oriented in the same direction. It has a thermal conductivity of 3.0 W/cm at 293K, which is greater than all other substrates and III-Nitrides. It has a lattice constant of 3.081Å and thermal expansion coefficient of 4.46×10^{-6} K^{-1}, leading to the lowest mismatch with GaN of the commercially successful substrates in both cases [21], [22]. Aside from deposition on native material substrates, 6H-SiC devices offer the highest performance available. A sample calculation and illustration for epitaxy of GaN can be seen in fig. 7.

$$\frac{a_{GaN} - a_{SiC}}{a_{SiC}} = 3.5\%$$

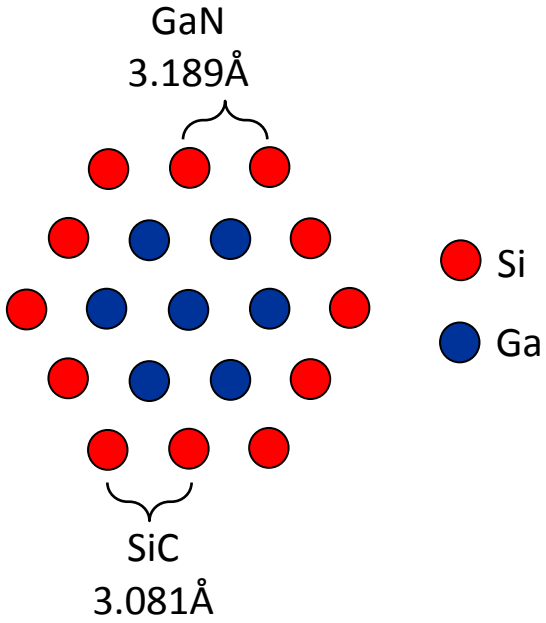

Figure 7: epitaxial relationship and lattice mismatch of 6H-SiC with GaN.

Bulk growth of SiC wafers suffers similar issues to III-Nitrides in that it cannot be produced using well established liquid melt methods such as the Czochralski process. In the case of SiC, this is because it undergoes sublimation at pressures attainable by liquid melt processes. Heteroepitaxial growth of SiC on Si is possible, but always results in 3C-SiC with a high degree of defects due to the lattice and TCE mismatch between SiC and Si. Growth of commercial SiC wafers typically relies on vapour phase transport and is more expensive, lower quality and smaller diameter than Si substrates [23].

1.6.3 Silicon

Epitaxy on Si substrates typically uses the (111) plane due to the hexagonal shape formed by neighboring unit cells. The basic geometry of this is shown in fig. 8.

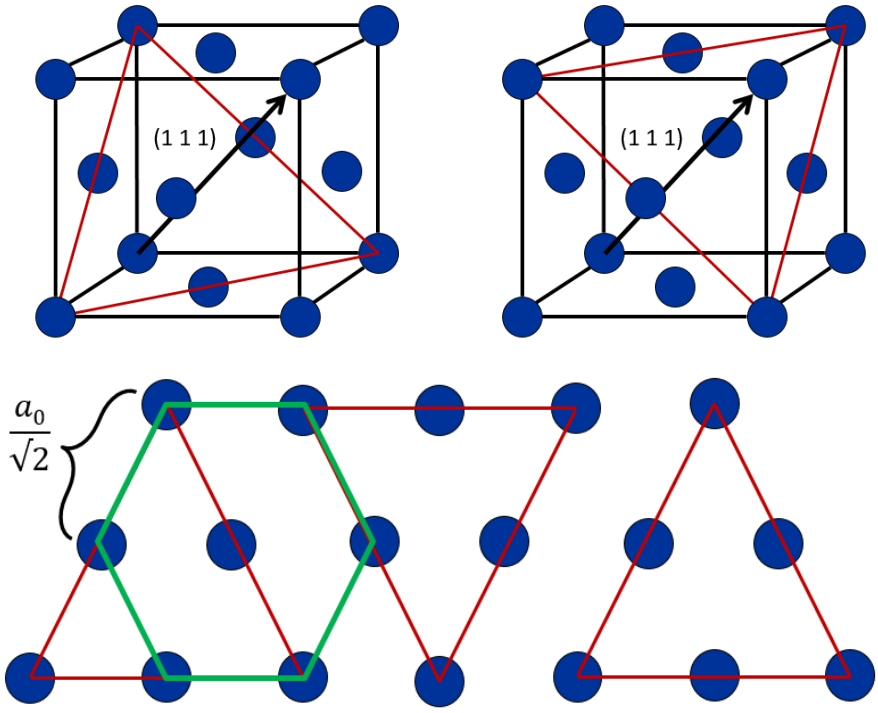

Figure 8: Epitaxial relationship between the hexagonal c-plane in III-Nitrides and [111] Si.

With a_0 for silicon being 5.431Å [24], this leads to a lattice mismatch with GaN of 17% and is comparable to sapphire. The mismatch with the TCE of GaN is also high. The chemical stability of Si can also present issues, as Ga can diffuse into the substrate and cause unintentional doping and melt-back etching of the substrate [25]. The relatively poor quality of Si as a substrate for GaN led it being developed chronologically latest. The major advantage of silicon is the large low cost wafers which can easily be produced, along with the ability to leverage established Si processes for wafer grinding and polishing, via-holes and die attach.

1.6.4 Glass

Deposition on glass substrates is attractive due to the highest area yields and lower costs possible. The use of glass as a substrate is widely used in display technology where high throughput is necessary and roll to roll processing is used. With display technology, ITO is commonly used as a front facing contact for thin film transistor technology in order to maintain transparency while still providing high conductivity. The processing of ITO is typically done at ambient temperatures and pressure in the mTorr range with a sputtering technique. Post deposition annealing is done around 200°C and results in smooth polycrystalline film with surface RMS roughness on the order of single nanometers. The polycrystalline film grain orientation is controlled by oxygen partial pressures during growth and preference of the (111) plane can be controlled by the amount of interstitial oxygen present in films [26]–[28].

Deposition on glass substrates is problematic because of the amorphous nature of glass and the large difference in thermal properties between glasses and III-Nitrides. A wide variety of glasses exist, some for specialty purposes such as alumino and borosilicate glasses, but the highest volume production glass is soda lime glass. This glass is produced from melting low cost

ingredients such as sodium and calcium carbonates (Na_2CO_3 and $CaCO_3$) and will be the main glass considered for determining physical and chemical properties of the substrate. The thermal expansion for this glass is $9.35x10^{-6}$ K^{-1} and the thermal conductivity is taken as 0.9 W/cm-K [29].

Because of the amorphous nature of glass, direct deposition leads to poor quality films an interfacing layer is required. The idea behind interfacing layers can be seen in fig. 9.

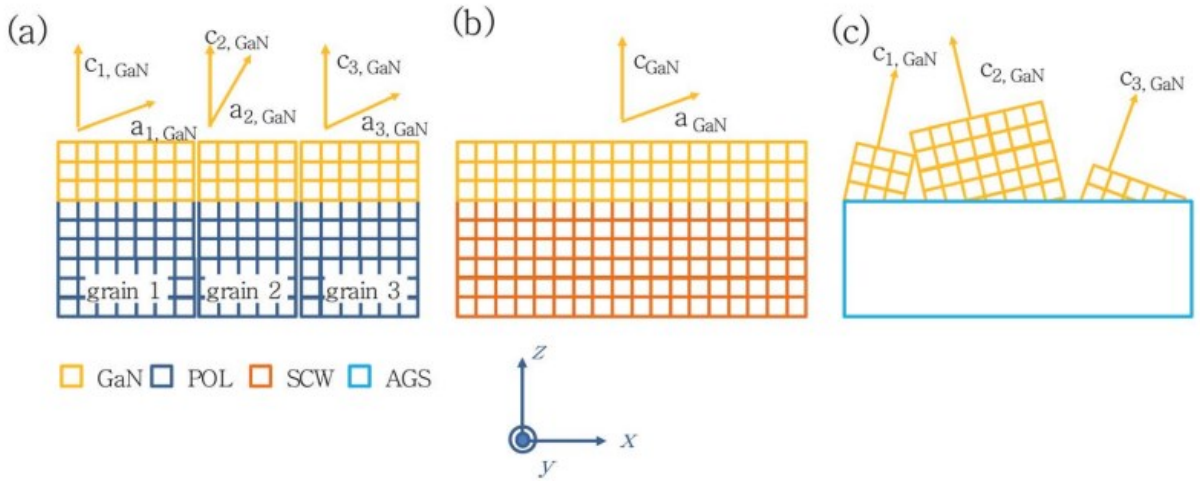

Figure 9: Epitaxy on glass results in 3 possibilities, a) a polycrystalline interface layer resulting in in multiple grains being formed with varying orientations, b) deposition on crystalline layers resulting an ideal single crystal and c) direct deposition on amorphous layers, resulting in misaligned growth vectors and amorphous growth [30].

The use of ITO as an interface layer is attractive because it leverages mature processing techniques found in display technology. Large area substrates of ITO sputtered glass can be purchased and the characteristics are well understood. Past research attempts have shown a variety of interface layers have been tried such as nickel, titanium, copper, silver, aluminum doped zinc oxide and ITO [31]–[33] for GaN and InN growth. Growth attempts of GaN have shown optimal temperatures of 430°C, which is suitable for low temperature processes needed for InN [34]. The thermal expansion and conductivity for ITO were taken as $7.23x10^{-6}$ K^{-1} and 0.4 W/cm-K for calculations [35], [36].

Chapter 2: III-Nitride Growth Review

Chapter 2 focuses on the growth technology used for III-Nitrides. The purpose of this chapter is to outline how the concepts of heteroepitaxy as outlined in chapter 1 are implemented in reality. This chapter provides an understanding of what growth techniques exist, what their operating principles that make them unique and their limitations.

2.1 Two stage growth techniques

The first growths of high quality GaN were performed in 1986 by H. Amano et al. utilizing a two stage growth process where a thin layer of low temperature AlN (900-1000°C) was on a sapphire substrate followed by a high temperature growth of GaN (950-1060°C) [18]. This was the first example of a two stage growth resulting in smooth GaN layers and led to a resurgence of research in the field of nitride semiconductors (fig. 10).

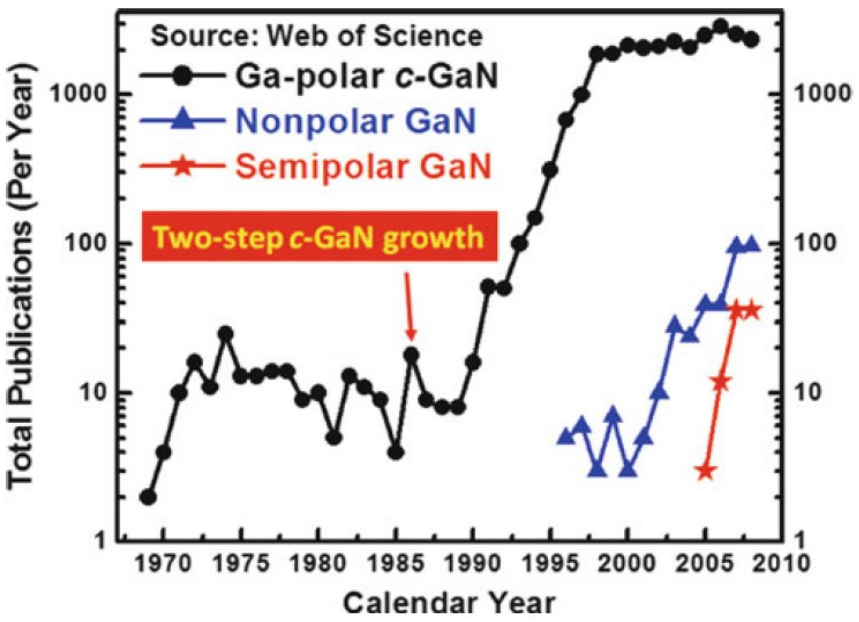

Figure 10: The discovery of high quality GaN growth techniques in 1986 led to their development as a key research material [37].

The new promise of quality GaN layers led to two stage growths utilizing low temperature GaN buffer layers and the development of p-type GaN using Mg as a dopant [38]. Since then it has become standard to utilize a multilayer buffer structure to filter dislocations and balance or compensate thermal mismatch between the substrate and deposition layers.

2.2 Nitridation

Nitridation is a general term that refers to exposing a surface to nitrogen and incorporating in the material [39]. The nitridation process has been shown to improve surface morphology as well as electrical and optical properties in low temperature growths of GaN on sapphire [40].

2.3 Growth Techniques

A wide variety of growth techniques have been used for the synthesis of nitride semiconductors, each with its own strengths and weaknesses. The following section provides a description of techniques used, their relevant chemistry and physical operating conditions and an overview of techniques used for low temperature epitaxy on ITO glass.

2.3.1 HVPE

Hydride Vapour Phase Epitaxy (HVPE) is a chemical vapour deposition (CVD) technique which utilizes HCl vapour to react with solid or liquid elemental sources to transport

III-Chloride vapour to a substrate chamber. The initial precursor reaction can be written for GaN as:

$$2HCl + 2Ga \Rightarrow 2GaCl_2 + H_2$$

Hydride vapours (AsH, PH and NH) are used as the group V sources. The resulting growth chemistry for GaN in the chamber can be written as:

$$GaCl + NH3 + H_2 \Rightarrow GaN + HCl + 2H_2$$

HVPE chemistry is advantageous in the elimination of carbon contaminants, but the production of HCL as a byproduct can be detrimental to the reaction vessel. HVPE has utility in its high growth rates, but the overall process lacks the control to produce thin layers for quantum well and super lattice structures for modern devices. Though HVPE is not suitable for modern device layers, its high growth rate has found use for non-polar orientation growth of bulk GaN substrates by growing of thick c-plane layers and cutting on an angle [41].

2.3.2 ALD

Atomic layer deposition (ALD) is a method based on sequential self-limiting half reactions cycled in loops to achieve high quality high precision conformal layers. The key advantage of high conformity and uniformity comes from utilization of surface saturation during each half cycle. As long as sufficient time is allowed for saturation, the type of reactants, substrate and temperature have significantly less impact on the overall deposition than other

techniques. The surface controlled growth however requires intermediate purging of the chamber between half reactions to avoid unwanted vapour phase reactions. A full ALD cycle of GaN would consist of:

i. The introduction of TMGa as the first reactant. The TMGa is chemically adsorbed by a previous nitrogen surface treatment, leaving $(CH_3)_2Ga$ bonded to the surface.
ii. A purge or evacuation via and inert gas to remove the non-reacted precursors and the gaseous reaction by-products.
iii. A nitrogen source is introduced. Nitrogen produced via thermal decomposition of NH_3 or a nitrogen plasma which reacts with $(CH_3)_2Ga$ by replacing the leftover methyl ligands. Each surface nitrogen atom is left with a dangling bond for the next TMGa step.
iv. A purge or evacuation.

The additional purge steps and requirement of surface saturation limits growth rates achievable by this method. The achievement of a limiting growth rate per cycle with this technique is indicative that surface saturation has occurred during each cycle and is commonly reported for this style of growth. Because of the limited growth rate this deposition method is typically only seen when high quality thin films are required, such as dielectric layers in FET devices.

2.3.4 MBE

Molecular Beam Epitaxy (MBE) is an ultra-high vacuum (UHV) deposition technique where molecular beams deposit thin epitaxial layers. The molecular beams are formed via thermal evaporation of elemental sources in effusion cells in the high vacuum. Because of the

high vacuum, the evaporated elements have long mean free paths compared to the chamber dimensions. This gives them a beam-like path in the vapour phase and is necessary avoid parasitic gas phase reactions of elemental vapours and ensures high purity layers. The beam trajectory and flow rate are controlled by the temperature and geometry of the cells. The effusion cell typically contains a crucible, a heating element and cooling element for thermal isolation and a mechanical shudder.

Because of its use of elemental precursors, MBE can be thought of as a physical vapour deposition technique, no precursors are necessary and chemical reactions do not occur. This is advantageous in the elimination of hydrogen and carbon complexes that can occur with CVD processes. Deposition of III-V nitrides in MBE can use ammonia as a nitrogen source, however from fig. 11 the thermal requirements of ammonia as a nitrogen source can be seen to require temperatures above 600°C. The thermal expansion of deposited layers can cause unwanted stress and defects in layers as well as difficulty in synthesizing high indium content alloys.

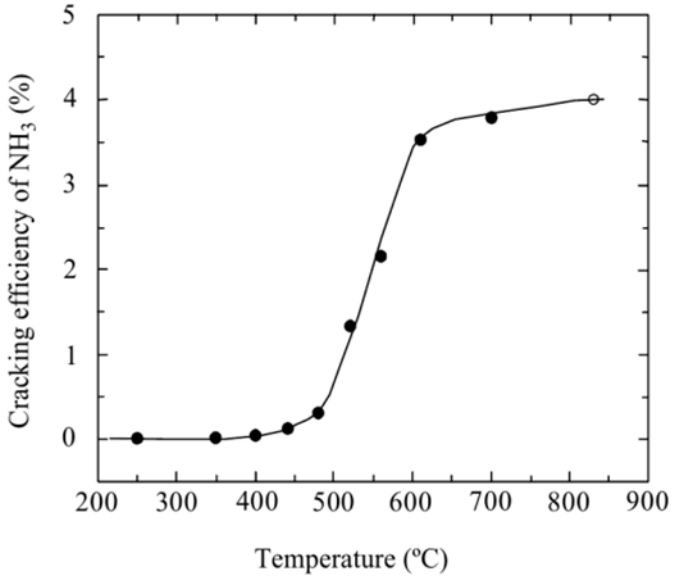

Figure 11: Thermal decomposition efficiency of ammonia. The sudden onset of cracking efficiency sets a lower limit on temperature in nitride growths [2].

Because of the control offered by the effusion cell, the high vacuum environment and the lack of chemical complexes, MBE offers high control over alloy compositions in binary and ternary structures as well as very high quality quantum well and super lattice structures. The UHV environment also makes this process suitable for many in-situ growth measurements, such as Reflection high-energy electron diffraction (RHEED) measurements, and has been historically valuable to researches seeking to understand the kinetics of crystal growth and in the design of novel device structures. While MBE offers great benefits in quality and control, the high vacuum requires relatively expensive equipment and it offers limited growth rates, which limit its scaling for commercial production.

A sample MBE chamber can be seen in fig. 12. Several effusions cells can be seen in the diagram, each with an individual shutter and line of sight to the substrate. A typical setup for a RHEED gun can be seen, with the electron beam at a glancing angle to the substrate surface. The liquid nitrogen cryopanel is a design feature in UHV systems and though common, is not specific to MBE. The chamber exit and main valve can be seen on the right hand side of the figure.

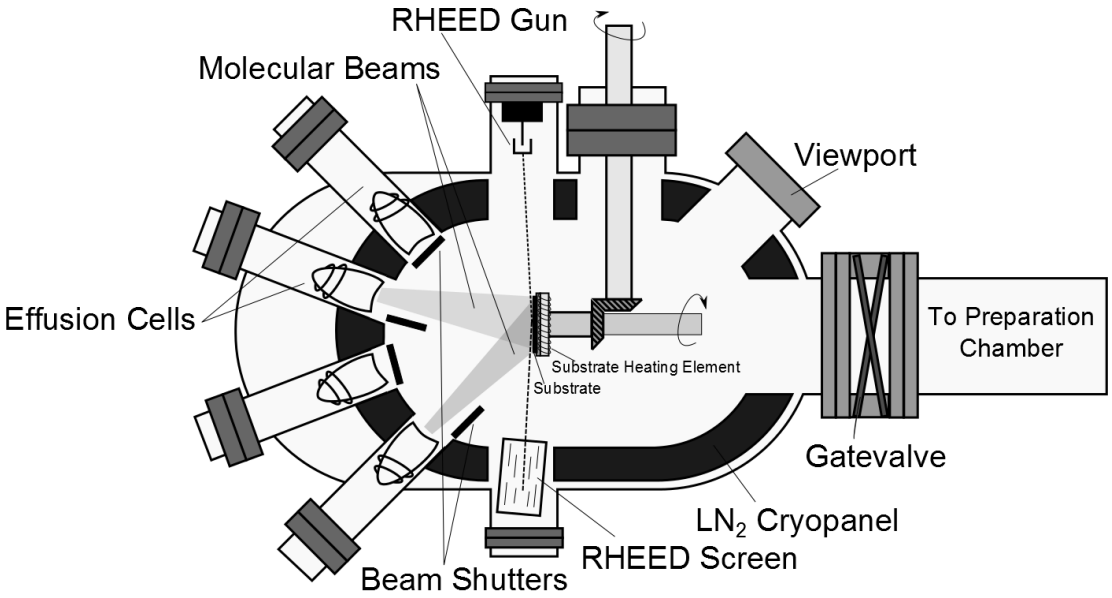

Figure 12: Typical MBE deposition chamber [42].

2.3.5 MOCVD

Metal-Organic Chemical Vapour Deposition (MOCVD) is deposition technique similar to ALD but relies on the full thermal decomposition of metal-organic precursors. The precursors used in this technique consist of metal-organics, which contain a metal carbon bond. These are typically trimethylaluminum (TMAl), trimethylgallium (TMGa) and trimethylindium (TMIn) in the case of nitrides, however a wide variety of precursors exist. The nitrogen source has historically been ammonia and as with MBE techniques, the decomposition of it is the thermally limiting reaction.

MOCVD operates at moderate pressures compared to MBE and higher temperatures compared to ALD. The higher temperature is used for the full pyrolysis of the metal-organic precursors, as opposed to the ligand exchange that typically occurs in ALD. This means the deposition reaction is not surface limited and many reactions occur in the gas phase within the chamber and on the surface.

The higher pressure and temperatures present result in a boundary volume above the substrate. Inside this boundary region the vapour phase decomposition of the precursors occurs. The presence of this boundary layer results in three distinct growth regimes for this deposition method. At low temperatures the growth will be limited to the rate at which the metal-organic ligands can be removed from the metal atom. This rate is described by the Arrhenius equation and in these temperature ranges the growth is said to be kinetically limited, as the boundary layer is sufficiently thin that diffusion across it occurs quickly. As the temperature increases, the convection of heat from the substrate causes a greater number of precursors to become activated at further distances from the substrate, extending the boundary region. As the boundary region grows the diffusion of precursors takes more time and eventually the diffusion time is

sufficiently long enough that it becomes the limiting step of growth. This is referred to as the diffusion limited regime. As the temperature is further increased the deposition rate begins to be dominated by evaporation and parasitic vapour reactions, eventually leading to a decrease in growth rate. The limit of these growth regimes varies between precursors and deposition pressures.

MOCVD has several advantages compared to other deposition techniques. Since CVD utilizes vapour phase chemistry with the substrate surface, it is not limited to line of sight like physical deposition techniques and can produce uniform layers on complex geometries and high aspect ratio features.

2.4 Plasma Assisted Growth

Regardless of the deposition techniques used, ammonia has historically been used as a source of nitrogen for nitride semiconductor growth. The use of ammonia forces a lower limit on the growth temperatures for achieving reasonable levels of nitrogen incorporation in a crystal lattice, as sufficient thermal energy must be supplied to the gas to break the N-H bonds. When these materials are synthesized at lower temperatures there is often a high level of background donors due to nitrogen vacancies. This only adds to the difficulty of producing intrinsic and p-type layers. An alternative to this is to provide the energy to a nitrogen molecule via an electric or time varying magnetic field. The advantage of this is greatly increased reactivity at low temperature for nitrogen gas and for nitride semiconductors an overall lower growth temperature can be achieved.

Nitrogen plasma can be created by passing nitrogen through a high enough field to ionize the gas molecules. The velocity of electrons in the plasma follows a Maxwell-Boltzmann

distribution and some fraction of electrons will have enough energy to dissociate nitrogen molecules, leading to reactive molecular nitrogen and atomic nitrogen species in addition to a small content of ionic species.

The electrons released from ionization are of high energy and are commonly referred to as “hot” electrons because their kinetic energy is effectively what it would be if they were thermionically emitted. The kinetic energy of the gas atoms is small by comparison due to their relative mass and the overall temperature of the system is significantly lower than the electron temperature. The non-equilibrium condition of the hot electrons results in a special boundary condition known as the plasma sheath. Because of the high kinetic energy of the electrons, they expand from the plasma at a greater rate than ions and negatively charge all surfaces in contact with the plasma. The potential difference of the plasma bulk and the surface reaches a steady state when the attractive force of the ions counters the effects of the hot electron flux on the bounding surface. This potential difference accelerates the ions and depending on their resulting kinetic energy can have several effects on plasma assisted growth. These effects are outlined in fig. 13 [43].

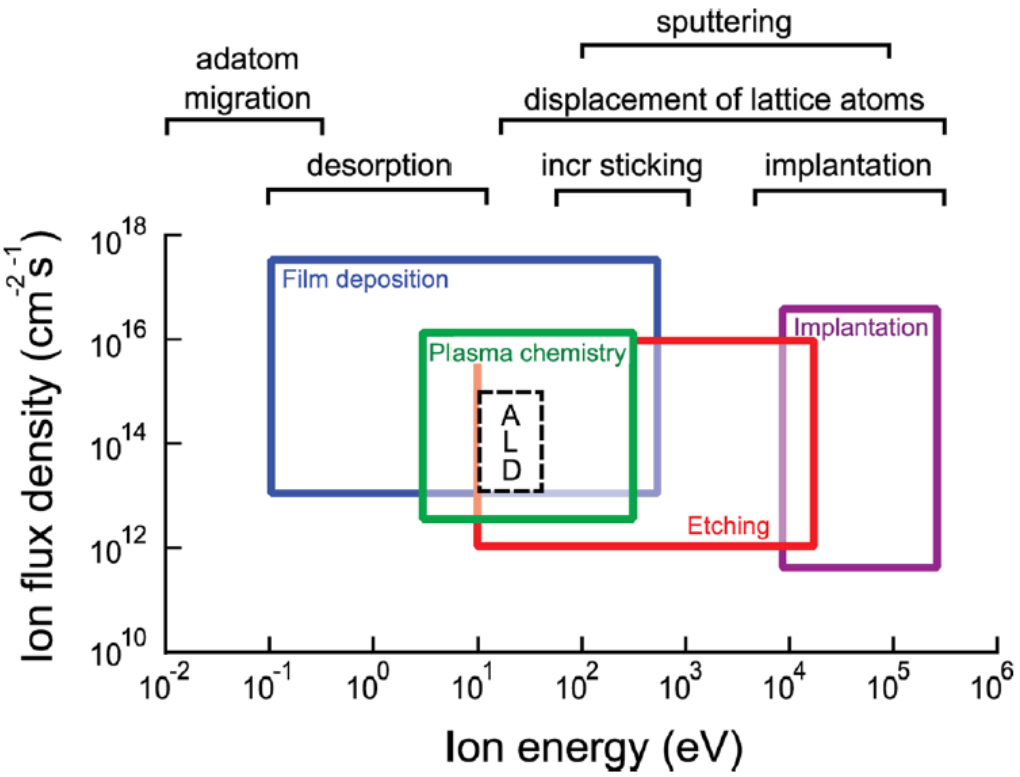

Figure 13: Possible effects of high energy ions on ALD growths. These effects are not specific to ALD and directly apply to both MBE and MOCVD techniques.

The effects of these ions varies from being beneficial at low energy, assisting in adatom migration during deposition, to etching and implanting ions at higher energies. Depending on the composition of the plasma, the mass of the ionic species may allow ion energies to span multiple regimes. It has been demonstrated in literature that H_2+N_2 mixtures of plasma provide higher quality growth than pure nitrogen in nitrides for this reason [44].

The reactive species can be utilized as a source of nitrogen for nitride growth, but the role of each species may not be intuitive. It may be expected that growth rates observed could be correlated to the concentration of atomic nitrogen species in the plasma, as each nitrogen atom in the wurtzite lattice is bound to four metal atoms, but this is not observed in nitride growth [45]. The relative concentration of nitrogen species can be determined via a spectrometer, as each

species emits a distinct wavelength based on discrete energy levels in nitrogen. Control of the plasma composition can be accomplished by changing the power for generating plasma and the pressure of the chamber during plasma generation. This adds an additional degree of control for researchers in designing deposition processes that is not possible with thermally activated nitrogen processes.

2.5 Lakehead Reactor

The Lakehead experimental reactor is a modified version of a remote plasma metal-organic chemical vapour deposition (RP-MOCVD) reactor. The system consists of three individually pumped chambers, a plasma source, a gas cabinet and control panel.

The three chambers consist of a residual gas analysis chamber, a load locking system and the main deposition chamber acting as a hub for the other chambers. Each of the chambers has a mechanical rotary pump to provide necessary background pressure for the high vacuum turbomolecular pumps (Edwards STPH301C). The system uses a standard UHV Conflat sealing system with copper gaskets.

Samples are initially loaded into the load lock onto the transfer arm. The use of a load lock system is common in vacuum systems and allows for loading and unloading of samples without depressurizing the main chamber. Pressures in the load lock are monitored using a MKS instruments baratron sensor and the main control panel. The gate valve separating the load lock from the main deposition chamber is manually controlled on the main panel and in order to minimize pressure, is closed during deposition.

The main chamber pressure is equipped with several process monitoring tools, such as a pyrometer, thermometer, RHEED gun and a baratron pressure sensor. The RHEED system is not utilized during growth due to the growth high pressure being too high and the risk of contamination with the metal-organics.

Pressure in the main chamber is controlled via the baratron and throttling valve. Combined with the thermocouples and main heater coil, this fully automates pressure and temperature control during growths. Low pressure growth is beneficial for minimizing oxygen contamination in growths.

The main chamber also houses the hollow cathode plasma source. Since the initial patent the showerhead nozzle has been removed, but other reactor components has remained. The substrate holder pedestal is rotated during growth in an attempt to lower inhomogeneity due to the nozzle removal and reactor geometry.

The plasma source is similar to that of a capacitively coupled RF source operating at 13.56 MHz, but utilizes a hollow cathode geometry as opposed to a more conventional parallel plate system. This allows for electron densities of 9.0×10^{11} cm^{-3} [17] at 600W of plasma power, upwards of 50x typical densities in capacitive systems. In addition to this it avoids the use of quartz or alumina tubes found to introduce oxygen contamination in inductively coupled systems [17], [46]. The practical lower limit for growth pressures is limited by the density of gas needed by the plasma source.

The gas delivery system is housed in the gas cabinet and is controlled via the main control panel. A diagram of the gas panel can be seen in fig. 14. This system contains all the precursors used in III-Nitride growth as well as Bis(cyclopentadienyl)magnesium (CP_2Mg), a

common magnesium source used in MOCVD. Mass flow controllers are used to set a controlled limit on precursor flows into a vapour line that feeds into the main chamber when the desired valves are opened. The pneumatic valve system is powered by an ultra-high purity nitrogen tank to ensure a lack of contamination.

The system does not use a carrier gas but instead uses a controlled pressure on the vapour line to maintain flow into the reactor. The pneumatic valve system is unique in this reactor and allows for fast, on demand binary flow control through the vapour line by enabling a main chamber valve (PV-14, PV-17 or PV-20 on fig. 18) or a bypass valve (PV-13, PV-16 or PV-19 on fig. 18) with the desired bottle valve open. These can be modulated at a maximum 1Hz by the main control software. The pulsing of the precursors into the main chamber has been shown to be beneficial to thin film growth and reduces parasitic vapour phase reactions that can occur in conventional MOCVD. The valve timings are controlled at the main control panel and are predetermined by the growth recipe. By repeating cycles of pulses, thin film layers can be accumulated. A separate plasma line is connected to an external nitrogen tank in line with a flow controller. The flow of nitrogen is independent of the metal-organics and delivery of plasma can occur continuously or be pulsed by controlling the biasing voltage at the plasma head.

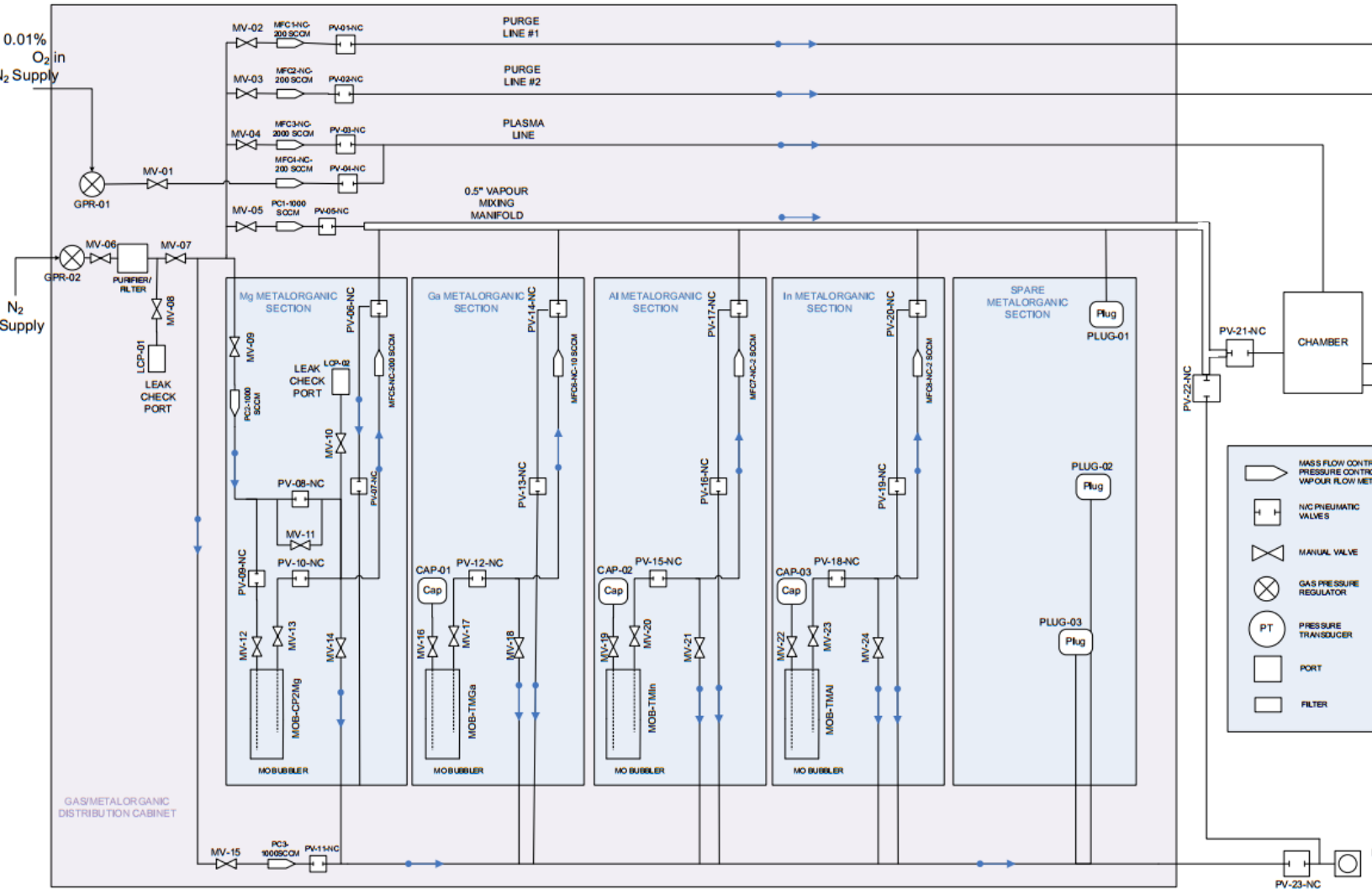

igure 14: The gas cabinet of the Lakehead experimental reactor. This cabinet controls all gas flow to main chamber through pneumatic valves and maintains temperature apour flow in the lines.

Chapter 3: Characterization Methods

Chapter 3 serves to outline the tools used in the analysis of chapter 4. Following chapter 3 an understanding of the results presented in chapter 4 should be more intuitive. Each tool has a theoretical outline followed information about the actual system used.

3.1 Atomic Force Microscopy

3.1.1 Theory

The AFM is a non-destructive surface characterization technique which can provide atomic scale resolution with great cost efficiency and speed with little sample preparation. In AFM measurements a small cantilever with a fine tip is mechanically positioned over evenly spaced points in a desired scan area in close proximity to a sample. At each point the vibrational movement of the cantilever is measured using a laser and photodiode array. Depending on the operating mode, different data is used to interpolate and map a false color plot of the sample surface. It is common in literature to report RMS surface roughness values as a metric of sample smoothness.

Key technical feats for the AFM are the ability to fabricate high precision tips on the cantilevers and control of tip positioning in three dimensional space on the order of one nanometre. Cantilevers are often fabricated using standard silicon photolithography technology, allowing precision control geometry and the ability to engineering tips with thin film coatings or specific stiffness. Positional control of the cantilever utilizes piezoelectric transducers for precise movement combined with stepper motors for macro scale movement of the scan head.

With AFM there are three general types of operating modes: non-contact, contact and tapping mode. In non-contact modes the cantilever is excited close to its resonant frequency and brought in close enough proximity of the sample to experience loading due to van der Waals forces. The loading acts to shift the resonant oscillations of the probe, which is monitored by the laser and photodiode array. A z-axis controller is then used to adjust the distance of the probe from the sample to shift the resonance back to original value. The controller response is used to determine the sample topology. The main advantage of this style of measurement is no contact is made and thus wear on the tip is minimized and sensitive samples can be measured. The main disadvantage is that surface contaminations such as water from ambient humidity may be falsely read as the sample surface. When using this technique a percent of vibrational amplitude is given to the controller to define what reduction in amplitude it can consider close to the sample. Specifying a lower percentage means a greater reduction in amplitude and a closer proximity of the probe to the sample. To minimize tip and sample wear the set point should be as large as possible. If the set point it set too large however, the controller may not be able to accurately follow the sample surface.

In contact mode the static deflection of the probe is used for the error of the z-axis controller. The z-axis controller adjusts the distance of the probe from the sample to maintain a constant repulsive force as the probe is dragged across the scan area. When using this technique a force set point is given to the controller to define a deflection. In addition to this, the probe stiffness properties must be specified to the controller to calculate the force based on the deflection. The force should be minimized in order to minimize wear on the probe and sample.

Tapping mode is an alternative to non-contact methods where the probe is excited to its resonant frequency with constant amplitude but is brought close enough to the sample to

experience contact forces from the surface. This technique has the benefit of inherent protection from tip-sample adhesion and false readings due to liquid contaminants that may be seen in non-contact mode, but at the same time decreases wear on the sample and tip compared to a contact mode.

3.1.2 Measurement Technique

Measurements were taken using an AFM Nanosurf Easyscan 2 atomic force microscope. The probes used were the ACLA model featuring aluminum top coating, a length of 225um, width of 40um, tip radius of <10nm, height of 14-16um and a stiffness of 36-90 N/m. A typical scan area consisted of 8.2um^2 with 1024 lines at a one second per line.

3.2 X-Ray Diffraction

3.2.1 Theory

XRD is a non-destructive, non-contact method of exploring the crystal structure in solid sample which relies on the constructive inference of diffracted x-rays within the crystal structure of the sample. Samples are placed in the path of a collimated beam of x-rays where the angle of incidence is scanned over a set range to determine which angles satisfy the Bragg condition.

Diffraction is a general wave phenomena that occurs when a wave encounters a series of regularly spaced scattering sites with a spacing on the same order as the wavelength of the incident wave. This is the reason why x-rays are required. X-rays are typically produced by heating a cathode material in a high electric field until electrons are boiled off and accelerated to a cathode material. The high energy electrons impinge on an anode material and relax from a

high energy state, releasing an x-ray. A common anode material is copper, where the energy transitions of interest takes place from the 2p orbital of the second L shell to the K shell. Two emission lines dominate x-ray production and are referred to as the k-alpha 1 (0.1540598nm) and k-alpha 2 (0.1544426nm).

When a sample is bombarded with x-rays, electrons at each atom are accelerated under the electric field of the x-ray. This acceleration causes the electrons to re-emit at the same wavelength isotropically. When multiple x-rays are re-emitted from many regularly spaced sites in the sample they may experience constructive interference provided the path length difference to the detector between two scattering sites is an integer of the wavelength. This ensures the waves will be in phase and is the origin of the Bragg condition for XRD. This can be written as:

$$2dsin\theta = n\lambda$$

Where d is the interplanar distance, theta is the angle of incidence of the x-ray relative to the surface normal of the plane, n is an integer and lambda is the wavelength of the photons. This condition assumes the incident rays to be parallel and in phase. A two dimensional case can be seen in fig. 15.

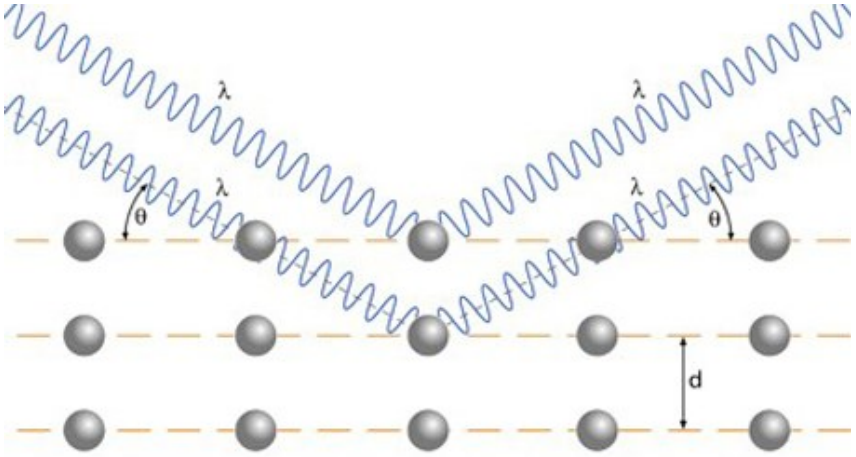

Figure 15: Bragg condition for x-ray diffraction [47].

With a description of the unit cell of a material the position of the diffracted peaks can be derived as a function of the lattice parameters. In a prefect single crystal material the constructive diffraction will only appear at exact angles from the Bragg condition. Factors such as strain in the lattice cause deviations in the interatomic spacing and distribution can be seen. A full width at half maximum can be measured in real samples to quantize the deviation from an ideal crystal. This is commonly reported in literature and a smaller FWHM generally results from a higher quality crystal. The absolute height of the peaks is not usually reported as it is a function of experimental conditions, such as the number of x-rays produced by the tool and will not be consistent [48].

3.2.2 Measurement Technique

All measurements were performed using the Lakehead university instrumentation labs PANalytical X'Pert Pro MRD in the w-2theta orientation. In this scanning type the x-ray detector and emitter are kept at the same angle relative to the normal of the sample (theta) and varied through a range at a rate w. The k-alpha 1 peak was used for the copper anode with an accelerating voltage of 40kV and a tube current of 40mA.

3.3 Scanning Electron Microscope

3.3.1 Theory

The SEM is a surface characterization tool which utilizes an electron beam and its interaction with a sample surface under a vacuum on the order of 10^{-4} Torr. The SEM is a

powerful tool that provides resolving power on the scale of 1nm with relatively little sample preparation compared to alternative techniques such as transmission electron microscopy. The focusing power is a result of the de Broglie wavelength of electrons being significantly lower than that of light, thereby lowering the diffraction limit of the beam spot. Fig. 16 shows a cross sectional view of the overall SEM system.

Electrons are produced through thermionic emissions under vacuum to increase their mean free path to practical lengths, accelerated under a high voltage and focused through a series electron lenses. The focal point is rastered over a sample area and a variety of detectors such as secondary electrons, backscattered electrons, Auger electrons and characteristic x-ray emissions. The K-alpha x-rays emissions for each element provide a signature of its presence and a chemical analysis can be performed by analysis of the energy dispersion in these emissions, known as energy dispersive x-ray analysis (EDX).

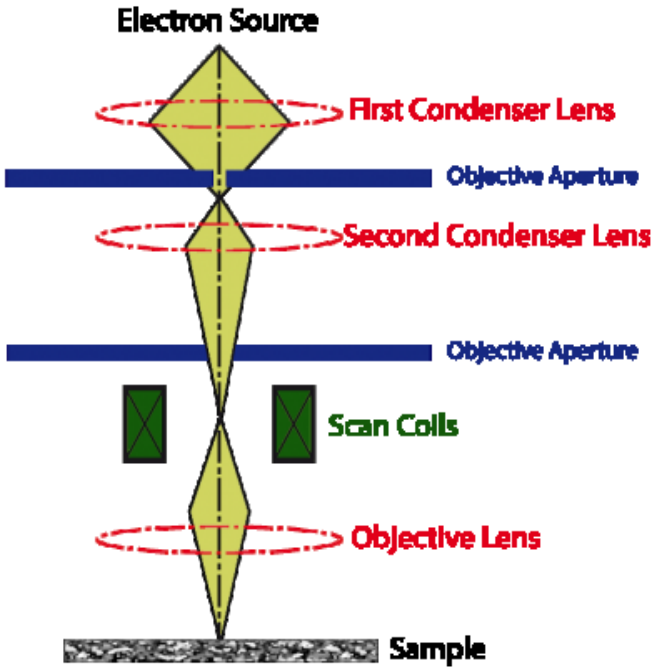

Figure 16: Cross sectional schematic of SEM operation [49].

3.3.2 Measurement Technique

Investigation of sample surface, cross section, layer thickness and chemical composition were all accomplished using the Hitachi SU-70 SEM located at the university. In order to investigate these properties sample were scored using a diamond tip scribe, broken and mounted on an SEM sample holder. A conductive carbon paint was used to increase the conductivity of the sample and improve image quality

3.4 Transmission Spectroscopy

3.4.1 Theory

Transmission Spectroscopy utilizes a range of light sources from the UV to IR to characterize the absorption of sample. From the characteristics of the absorption curve the thickness and band gap of a sample can be inferred.

When monochromatic light is shone on a semiconductor it can cause transitions of electrons to higher energy levels depending on the availability of states for transition. By sweeping through a frequency range the onset of photon absorption can be determined. The energy of the absorbed photon can be used to determine the band gap energy of the material, as no states are available for electrons until this threshold is reached.

The thickness of the sample can also be determined due to the effects of internal reflection. Reflection from internal surfaces in semiconductors samples can add constructively or destructively based on layer thicknesses and the wavelength of the photon. Since the thickness is constant, at certain wavelength the layer forms a basic fabry-perot cavity. This presents itself as

oscillations on the absorption plot. The thickness can be determined using the difference between two oscillations peaks by the following equation:

$$t = \frac{A}{2n\left(\frac{1}{\lambda_1} - \frac{1}{\lambda_2}\right)}$$

Where t is the layer thickness, n is the refractive index of the material and A is the number of periods between λ_1 and λ_2. If λ_1 and λ_2 are chosen as two adjacent maxima, A=1 and if a peak exists between λ_1 and λ_2 then A=2.

3.4.2 Measurement Technique

The instrument for this work was the Varian Cary 5e which can measure a range from 200nm to 1200nm. A full exposure and zero exposure baseline scan are taken for every measurement. The sample is placed between the source and detector and the absorption of sample is determined from the transmission spectrum. Thickness measurements will generally rely on SEM measurements.

3.5 Raman Spectroscopy

3.5.1 Theory

Raman spectroscopy is a spectroscopic technique which utilizes inelastic scattering of photons from a laser source to identify vibrational, rotational and other low frequency transitions in molecules. When the laser is shown on a sample there are three possible re emission mechanisms that occur based on the scattering the photons experience. The majority of photons

undergo elastic scattering and are simply reemitted at the same frequency as the laser light. This provides no information and is generally filtered out. A second possibility is that the photon excites a molecular vibration within the sample, loses energy and is re-emitted at a lower frequency. The third possibility is that the photon is absorbed by a molecule already in an excited state from a previous event. In this case it may experience an increase in frequency upon reemission. The shift in the frequency of the laser light is characteristic of the molecular bonds present in the sample and upon filtering the central frequency of the laser, information about the presence of specific bonds in samples can be obtained. This information may be useful for determining crystallographic orientations present in a sample [50].

Chapter 4: Growth Process and Discussion

Chapter 4 focuses on the data obtained. The chapter will begin by outlining the general procedure used for all materials and then branch into specifics for each system. This chapter will then use the information provided in chapter 3 to determine trends in data.

4.1 Glass Substrate Investigation

Glass substrates were purchased with ITO already deposited on the surface. Films were typically deposited using a low temperature technique resulting in amorphous films. The amorphous nature of these films was verified under XRD analysis in fig. 17 These films shows a characteristic shape of amorphous ITO glass [51].

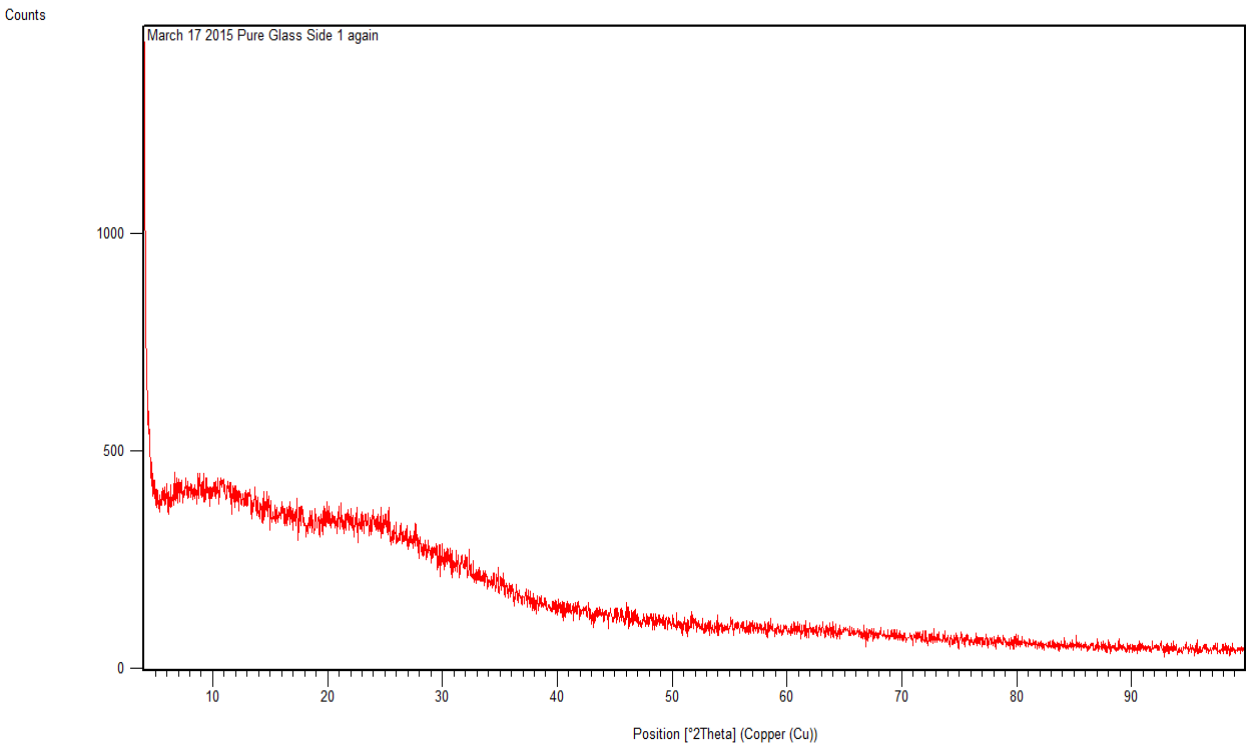

Figure 17: XRD scan of as purchased glass substrates.

Thermal annealing of the glass substrate was performed over 90 minutes at 450°C in nitrogen plasma under 100W of excitation power. The deposited thin films were shown to recrystallize and a characteristic InO spectrum can be seen in fig. 18. The highest peak is the (222) plane located at 30.96°. This plane is parallel to the (111) surface and presents the same distorted hexagonal In-In structure shown in chapter 1.

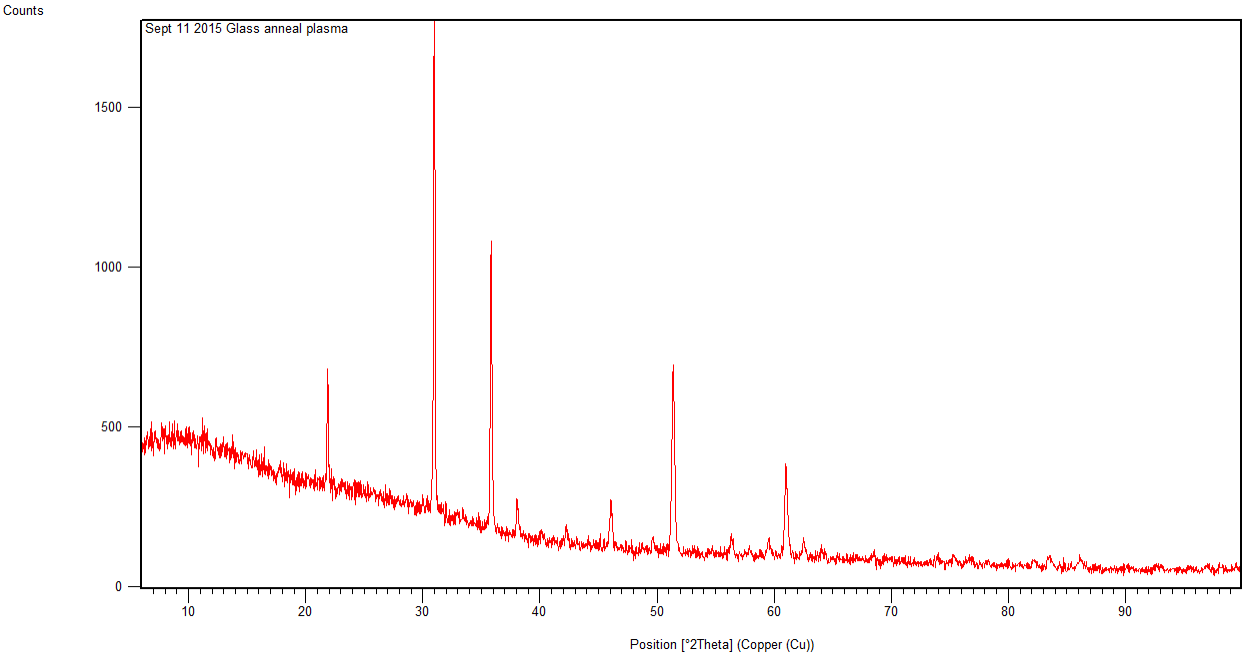

Figure 18: Annealed ITO glass spectrum. The dominant peak at 30.96° corresponds to (222) peak.

All growths were preceded with a nitridation step. This step should provide a template of nitrogen atoms for metal atoms and all post nitridation growth procedures were initiated with a metal-organic step.

Metal-organic pulse timings and pressure ratios are listed in tables 3, 4 and 5. The pressure ratios are defined as the ratio of the vapour line with respect chamber pressure and the pulse timing ratio is the ratio of on to off time of metal-organic delivery.

4.2 General Growth Procedure

All growth procedures follow a similar template:

i. The valve to the residual gas analyzer chamber is closed to avoid damage to the filament. Manual valves for the RHEED gun and its screen are always kept closed.

ii. Initial heating in vacuum. The heating rate was fixed at 10° per 30s step.

iii. Pre-growth nitridation of the growth surface. The nitrogen power was kept at 600W for AlN and GaN growths and varied between 100 and 600W for InN growths. The time was varied between 1 minute and 5 minutes.

iv. Pressure adjustment for growth. Nitridation and growth pressure were varied independently. This step is necessary as pressure cannot be instantaneous changed.

v. Pulse of precursor. For the growth of InN, the plasma was run continuously at the settings use for the nitrogen deposition step during the growth. This metal modulated epitaxy technique has been found to be beneficial for the incorporation of nitrogen in the InN lattice. For AlN and GaN growths the plasma was disabled during these steps to minimize powder formation. The mass flow was held constant for each material. The pressure in the vapour line varies between growths. Flow rates were optimized values taken from previous records.

vi. Pulse of nitrogen plasma. The pressure in the main deposition chamber is maintained with a constant flow of nitrogen through the plasma line. When nitrogen plasma is needed, a bias is applied to the plasma head. During this time the metal-organics are sent to the bypass line, their flow is never stopped to avoid latency in their flow.

vii. In the case of indium nitride, to prevent the accumulation of surface droplets a relatively long nitridation step is introduced after 20 deposition cycles. This was kept at 40s in length using the same conditions as the nitridation during growth cycles. This is not done for AlN or GaN growths.

viii. The previous steps are repeated many times to accumulate a thin film layer. The number of cycles can be changed to deposit a layer of a desired thickness based upon a known growth rate per cycle.

ix. A post growth nitridation was performed for to reduce metal droplets on the surface.

x. Cooling under vacuum. Vapour line and chamber are purged during cool down to ensure no leftover metal-organics in the line for the next growth.

xi. Residual gas analyzer valve is opened when cool down has finished.

4.3 Growth Preparation

The sample holder was cleaned between depositions of differing materials to avoid cross contamination of materials. Cleaning of sample holder is done with an aggressive rubbing with 120 grit sand paper, rinsing with deionized water and then methanol. Glass samples are kept a plastic container between growths. Prior to a growth they are rinsed in acetone to remove surface contaminants and immediately loaded into the load lock and placed under vacuum. Loading of the samples is using a magnetically coupled loading arm and a viewport on the side of the reactor.

4.4 Results for AlN

Initial attempts at growth of AlN proved unsuccessful, resulting in the underlying annealed ITO spectrum being the only observable XRD spectra. A summary of growths can be seen in Table 3. Samples 1, 2 and 3 were the only samples which showed the underlying thermally annealed ITO spectra. Samples 4 through 9 showed a spectrum similar to the non-annealed glass spectra seen in fig. 17. This may indicate that the ITO was removed during the growth.

An SEM surface image of sample 2 can be seen in fig. 20. The corresponding EDX spectrum can be seen in fig. 21. The EDX spectrum shows several distinct peaks, with only the peak located at 1.5 KeV corresponding to aluminum. The series of peaks located between 3 and 4 KeV are from indium and the peaks between 0 and 1KeV corresponding to carbon, nitrogen and oxygen respectively. The measurable presence of nitrogen combined with the lack of any AlN XRD peaks indicates the deposited layer is possibly amorphous aluminum nitride. The high amount of oxygen may be from both the ITO and substrate, or possibly just the substrate. It is difficult to distinguish from the surface scan.

An SEM surface image of sample 5 can be seen in fig. 22. The corresponding EDX spectrum can be seen in fig. 23. Despite the appearance of an ITO layer, no indium was detected in the EDX spectrum and the oxygen peak was noticeably lower, but still present. The cross sectional image and EDX combined with the XRD spectrum show amorphous aluminum nitride is present on the surface, but no ITO can be detected. This indicates the removal of the ITO layer happened before the deposition of AlN, possibly due to etching effects of the plasma, but no clear correlation between the plasma parameters and the removal of this layer can be seen.

The only sample to demonstrate crystallinity was sample 10. This growth was unique in that it was deposited on top of InN/InAlN based on the best InN growths. 5 cycles of InN identical to sample 22 in table 5 were initially deposited. The ternary compound was created by inserting an aluminum deposition cycle in the main deposition cycle of InN such that one cycle of the growth loop proceeded as follows:

i. 10 cycles of metal modulated indium nitride growth with identical parameters to sample 22 in table 5.
ii. A 40 second plasma nitridation step to avoid the formation of surface indium droplets
iii. 10 cycles of aluminum nitride deposition as outlined in table 3, sample 10.

This process was developed in an attempt to deposit InAlN outside the scope of this report, but was used as a template for AlN growth. The deposition of AlN in accordance with table 3 sample 10 was immediately performed after the InAlN deposition previously outlined. The resulting XRD spectrum can be seen in fig. 19. The largest peak at 35.6° corresponds to the (002) plane of AlN. This indicates c-axis oriented AlN has been grown. The inclusion of an InAlN buffer layer has demonstrated an increase in AlN quality.

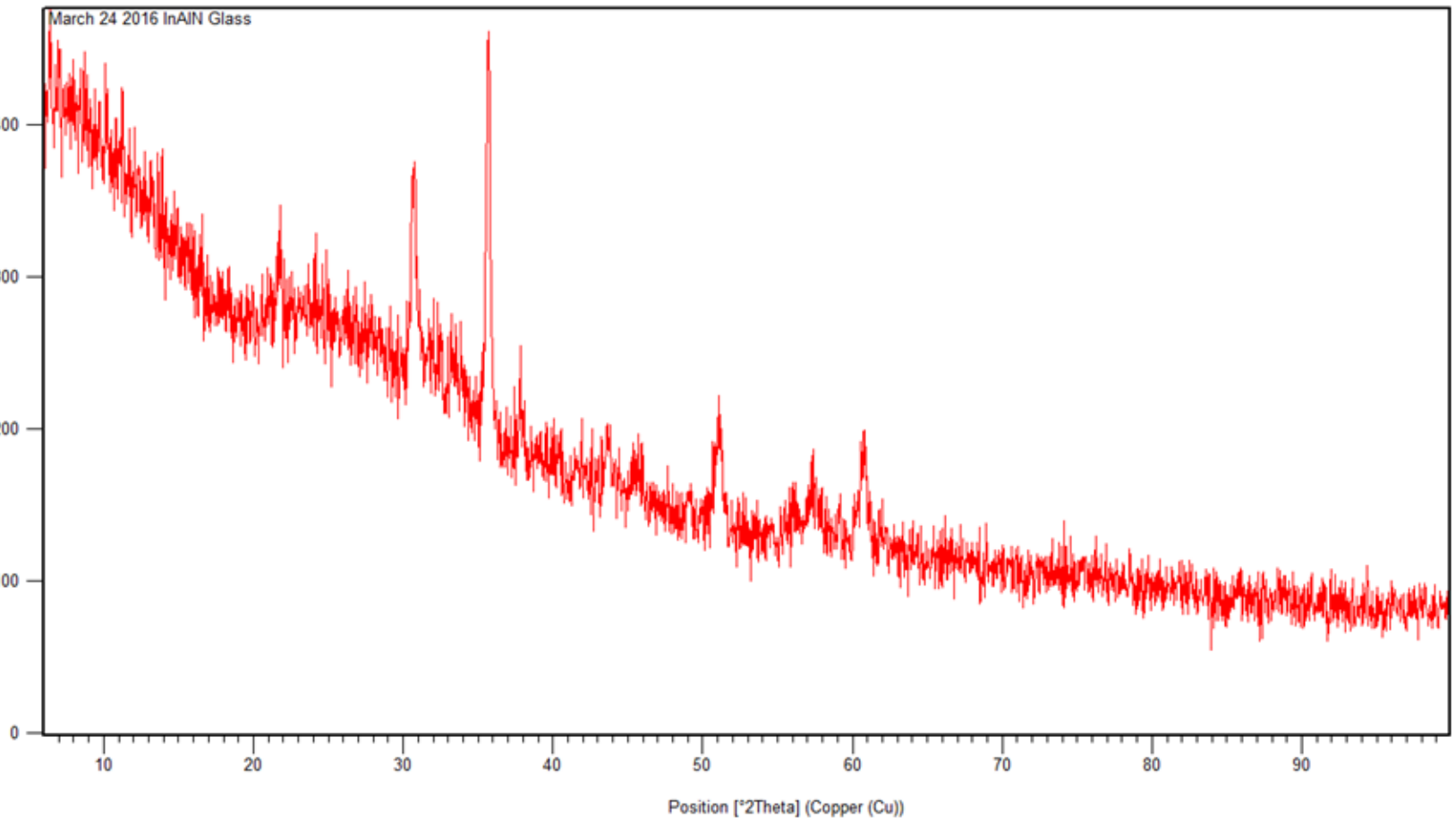

spectrum of AlN on InN/InAlN layer showing a peak corresponding to (002) AlN.

AlN Growth parameters.

	RPM	Cycles	Nitridation Time (s)	Power (W)	Nitridation pressure ratio	MO timing ratio	Deposition pressure ratio	Plasma Power (W)
	50	300	600	600	1.00	0.25	0.73	600
	20	400	60	600	1.00	0.4	0.73	600
	0	400	60	600	1.00	0.4	0.73	600
	60	400	300	600	1.00	0.4	0.73	600
	20	600	600	600	1.33	1	1.33	600
	60	100	120	600	1.33	0.6	1.33	600
	60	400	60	100	5.33	1	8.00	600
	60	400	60	100	5.33	1	5.33	600
	60	400	20	100	5.33	1	5.33	600
	60	300	60	200	3.33	1	10.00	200

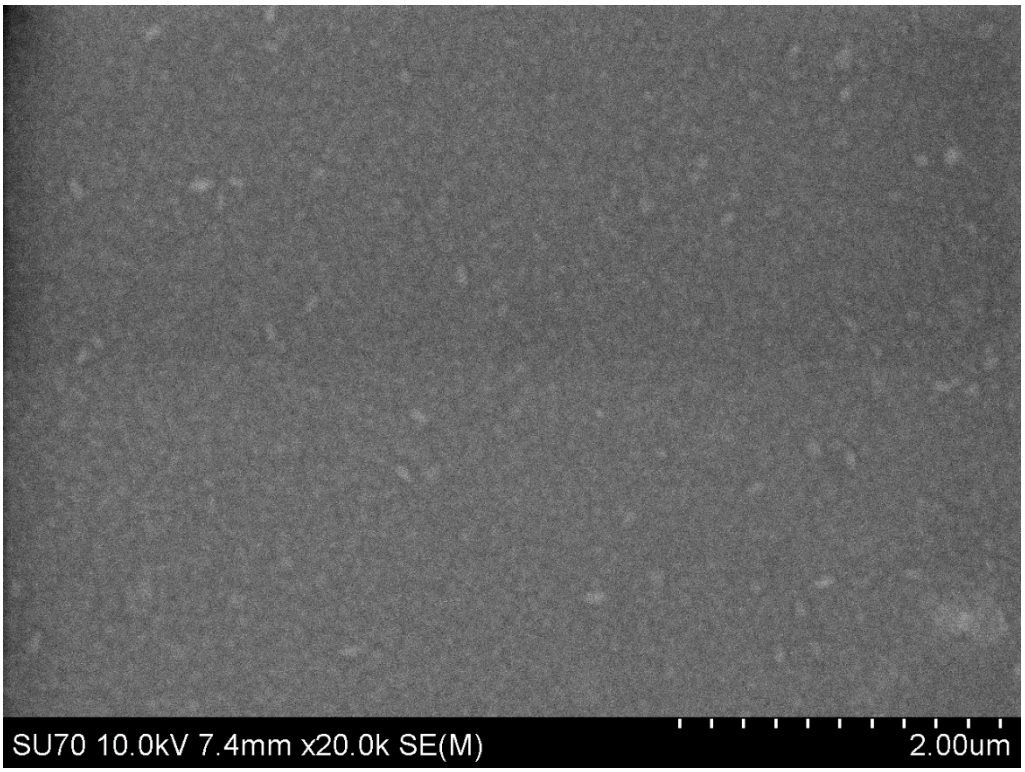

Figure 20: SEM surface image of sample 2.

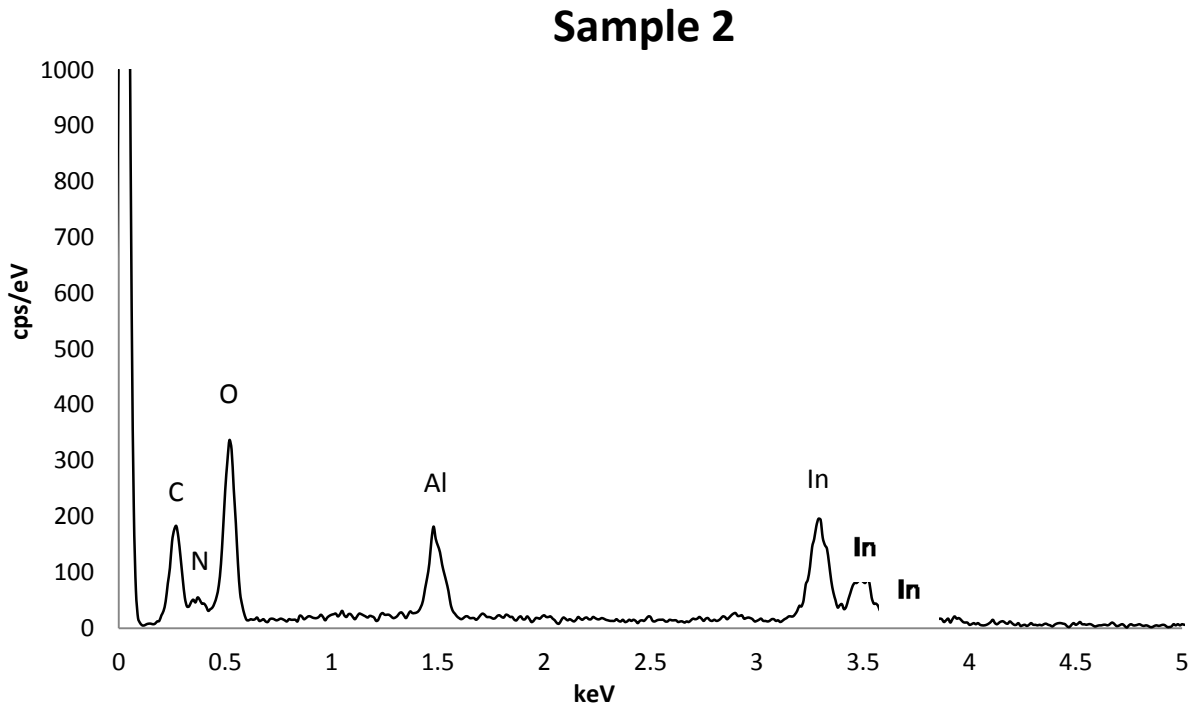

Figure 21: EDX spectrum of sample 2. This spectrum verifies the presence of indium oxide and aluminum nitride.

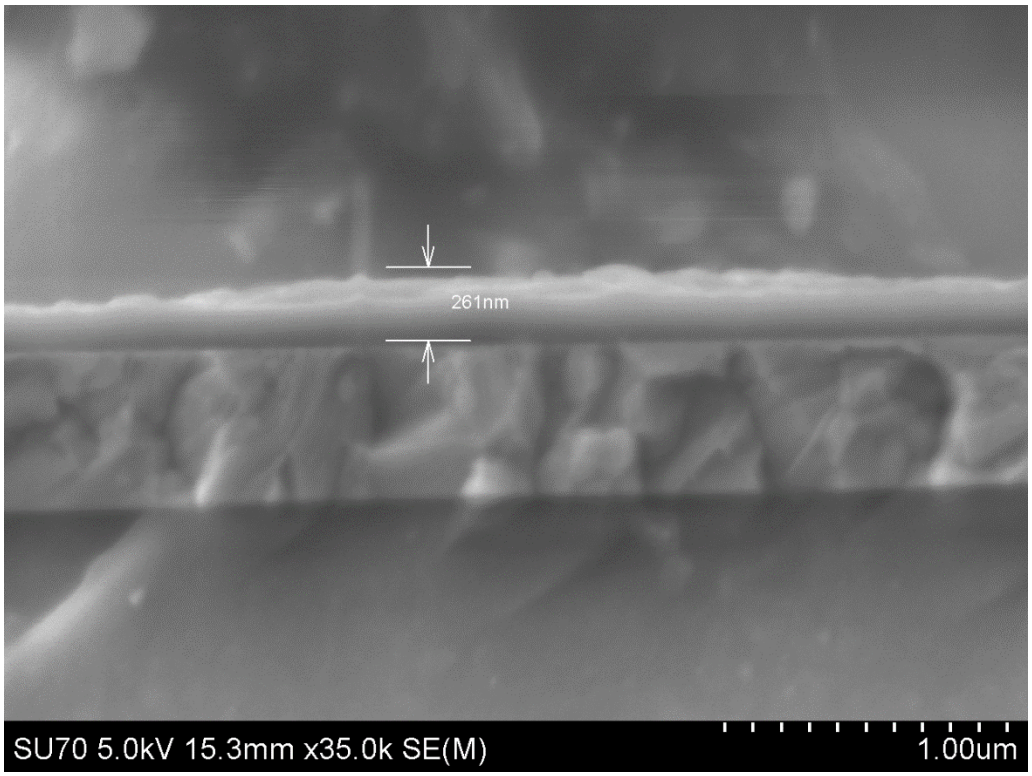

Figure 22: SEM cross sectional image of sample 5.

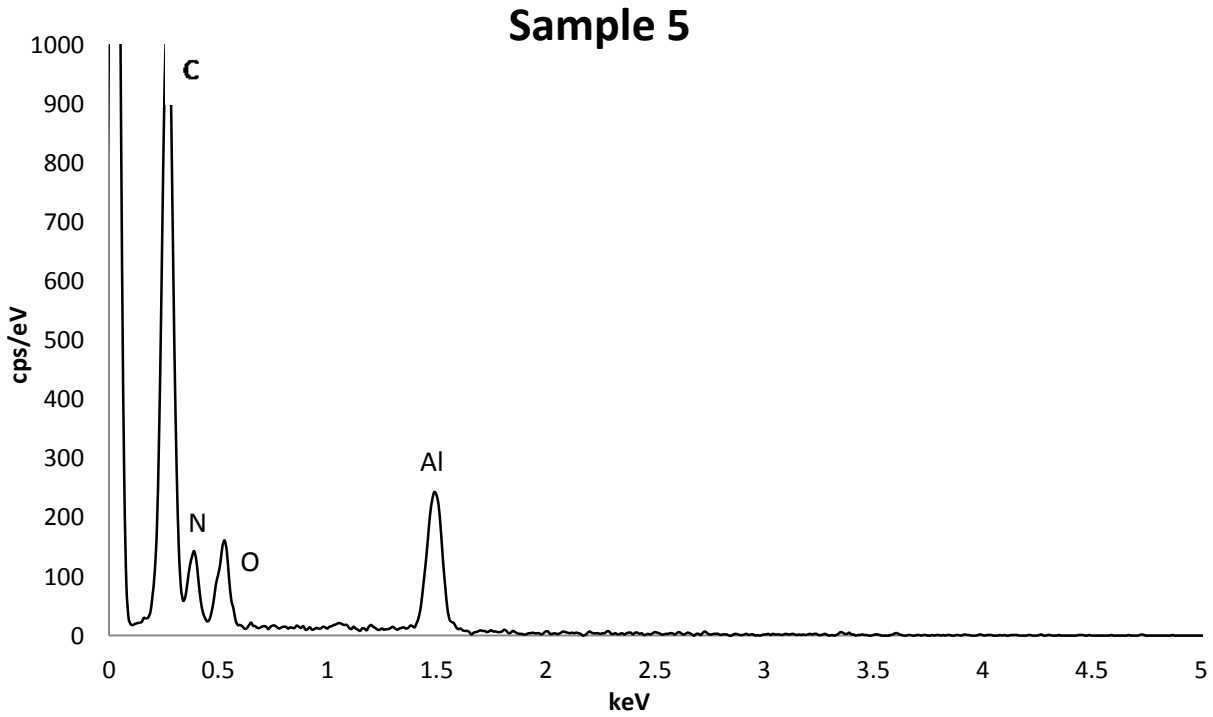

Figure 23: EDX spectrum of sample 5. There is a distinct lack of indium peaks present in sample 2, figure 23. The oxygen peak is also noticeably lower.

Absorption spectra for sample 5 can be seen in fig. 24. An interpolation of band gap reveals it to be close to 4.3eV. The results from the XRD, SEM and EDX show that this is most likely the band gap of the substrate. This type of measurement has limited results for AlN since the band gap is higher significantly higher than the substrate or the ITO interface layer. Even with ideal AlN layers, the absorption edge of the substrate will appear before the AlN.

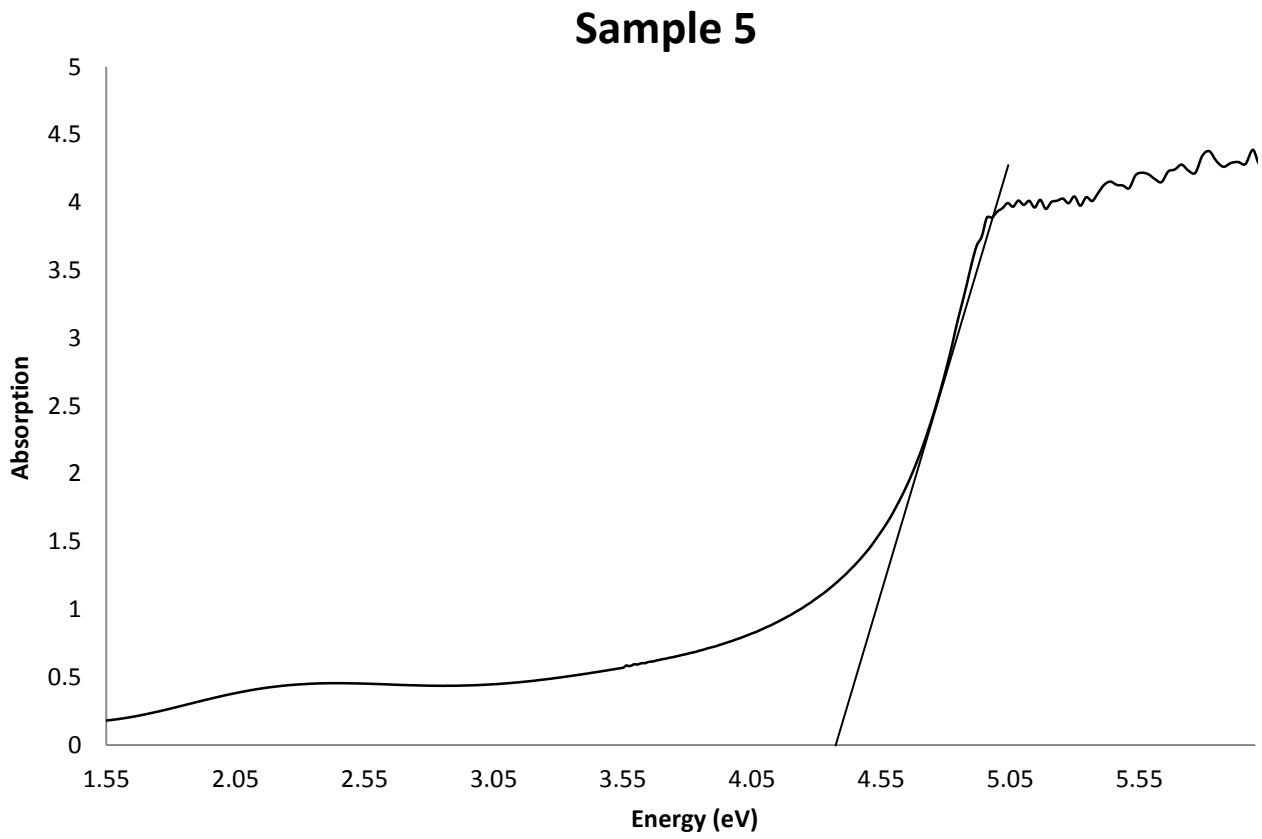

Figure 24: Absorption spectrum for AlN sample 5.

4.5 Results for GaN

Experiments for deposition on GaN are summarized in Table 4. The presence of GaN was not detected in any of the XRD spectra gathered, all spectra show a characteristic thermally annealed ITO curve identical to fig. 18. SEM and EDX analysis seen in fig. 25 and fig. 26 respectively show small amounts of GaN present on the surface. The lack of a GaN layer is most likely due to the pressure on the vapour line not being varied. Because the chamber pressure was high in comparison to vapour line, the pressure driven flow in the vapour line may have been insufficient for layer deposition.

Fig.27 shows the measured absorption spectrum of sample 7. The lack of a layer in the SEM results of fig.25 indicates this is most likely due to the glass. A linear interpolation of the absorption edge places it 3.8eV seen in fig. 24. GaN has an ideal band gap of 3.42eV, the absorption edge here is most likely due to glass because results from the EDX "Spectrum 1" spot indicating the layer has high levels of indium similar to fig. 21, while gallium is not seen. No distinct layer of GaN can therefore be seen in fig. 25.

AFM results for samples 1 through 5 and the thermally annealed substrate can be seen in fig. 28. The RMS roughness for the initial sample was 1807.7pm. After growth in samples 1 through 5 the roughness's were 939.71pm, 1503.7pm, 841.39pm, 1062.5pm and 1098.2pm. In all cases there was a decrease in the surface roughness from growth, though it is not expected that a substantial layer was deposited based on the results from sample 7.

ry of GaN Growth parameters.

	RPM	Cycles	Nitridation Time (s)	Power (W)	Nitridation pressure ratio	MO timing ratio	Deposition pressure ratio	Plasma Power (W)
	0	50	600	600	1.00	0.25	0.73	600
	0	50	600	600	1.00	0.25	0.73	600
	0	100	600	600	1.00	0.25	0.73	600
	0	100	600	600	1.00	0.4	0.73	600
	0	100	600	600	1.00	0.2	0.73	600
	0	500	60	600	1.00	0.4	0.73	600
	60	500	60	600	1.33	0.4	0.73	600

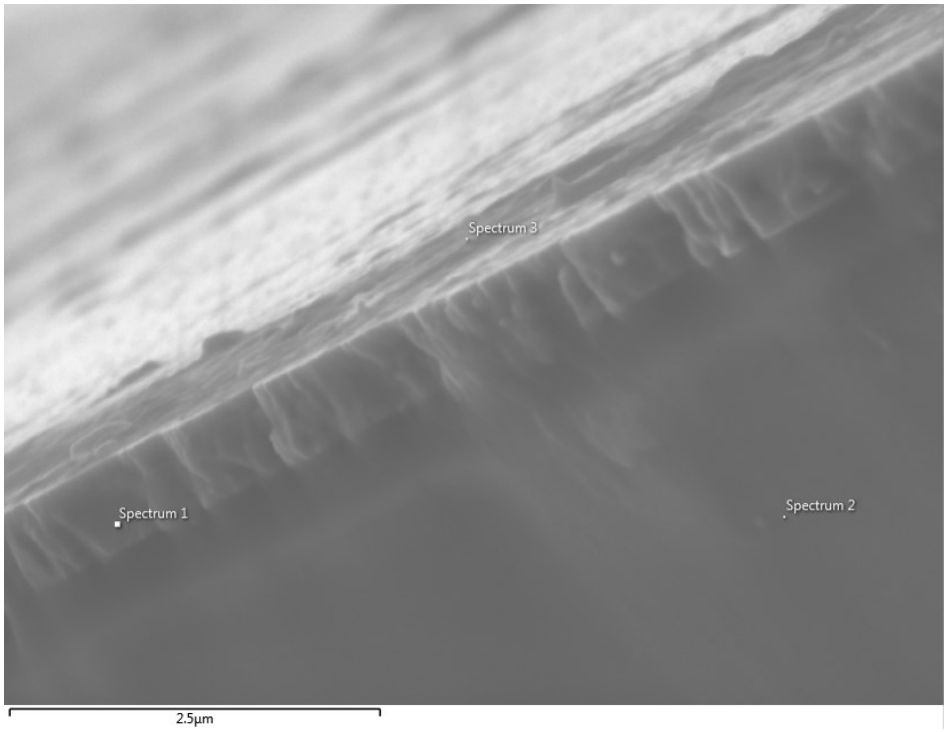

Figure 25: SEM image of sample 7 showing the cross section of the growth. The approximate thickness of the apparent layer was 600nm.

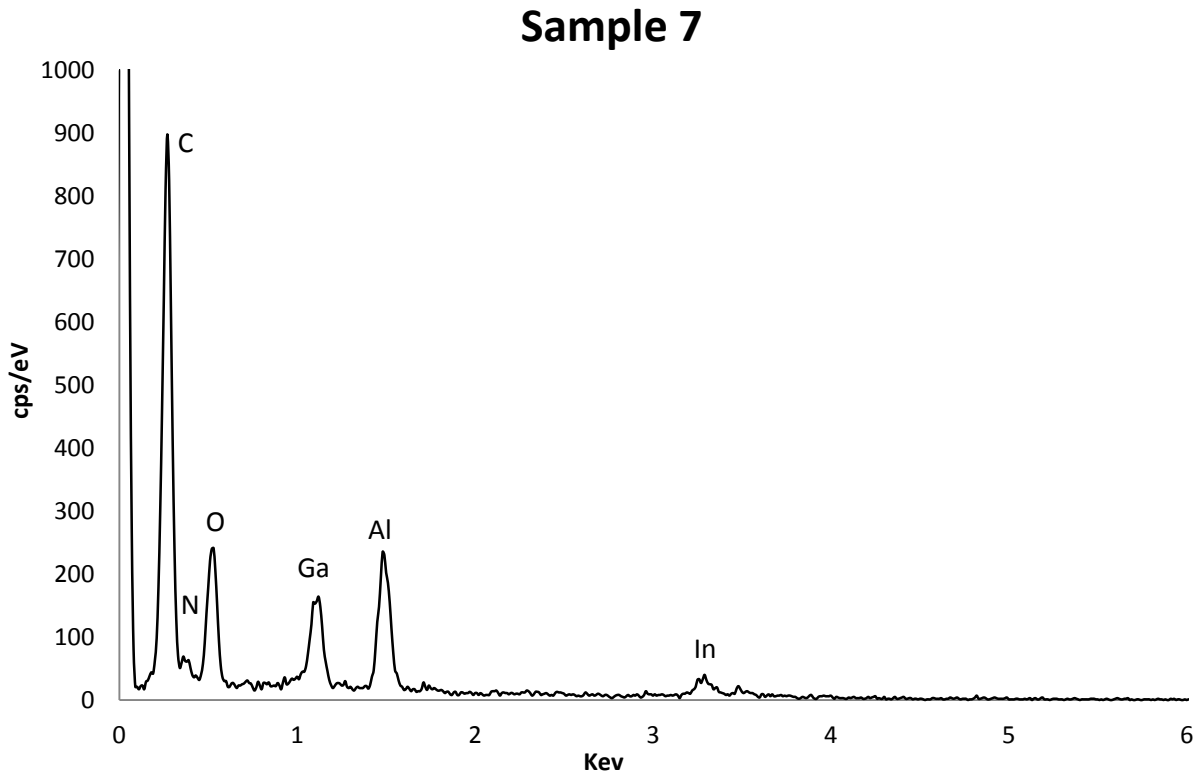

Figure 26: EDX spectrum of sample 7 showing an indication that gallium is present on the surface of the sample. This spectrum was taken from the spot label spectrum 3 in fig. 25.

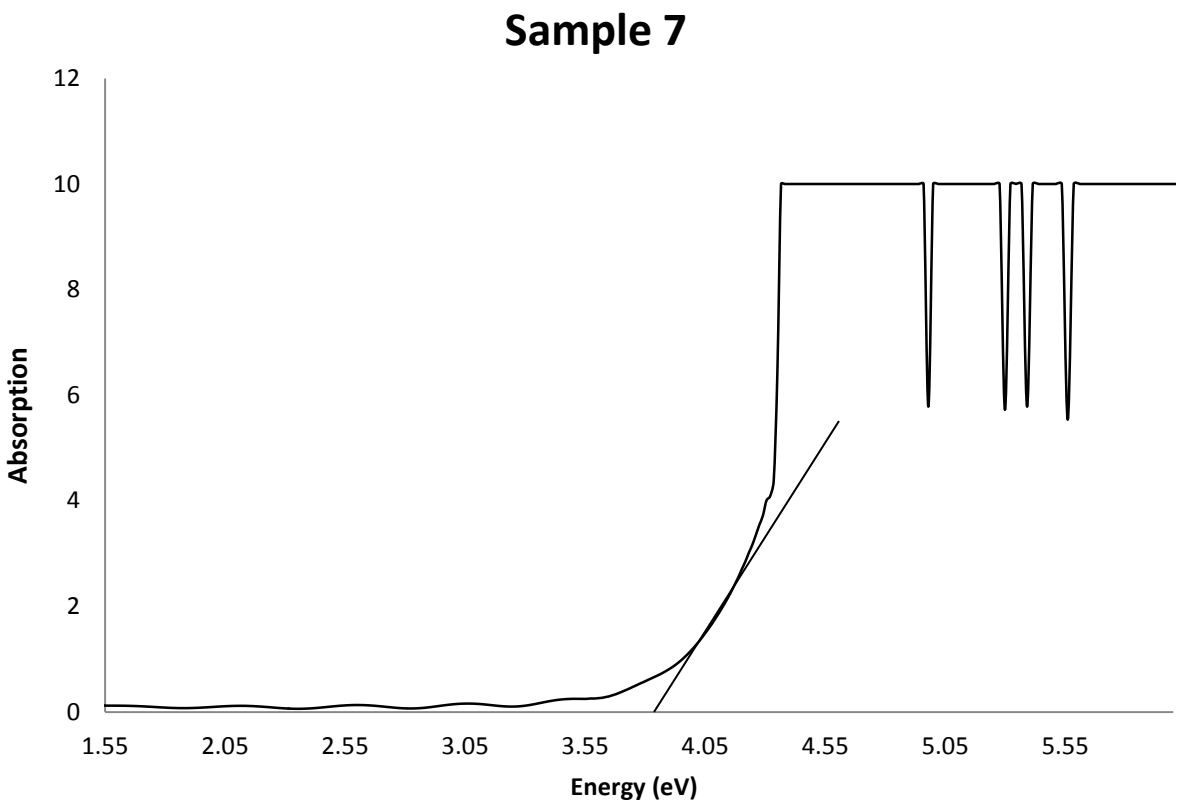

Figure 27: Absorption spectrum of GaN sample 7. A visual interpolation puts the onset of absorption in a similar spot as AlN sample 5 and most likely corresponds to the glass substrate.

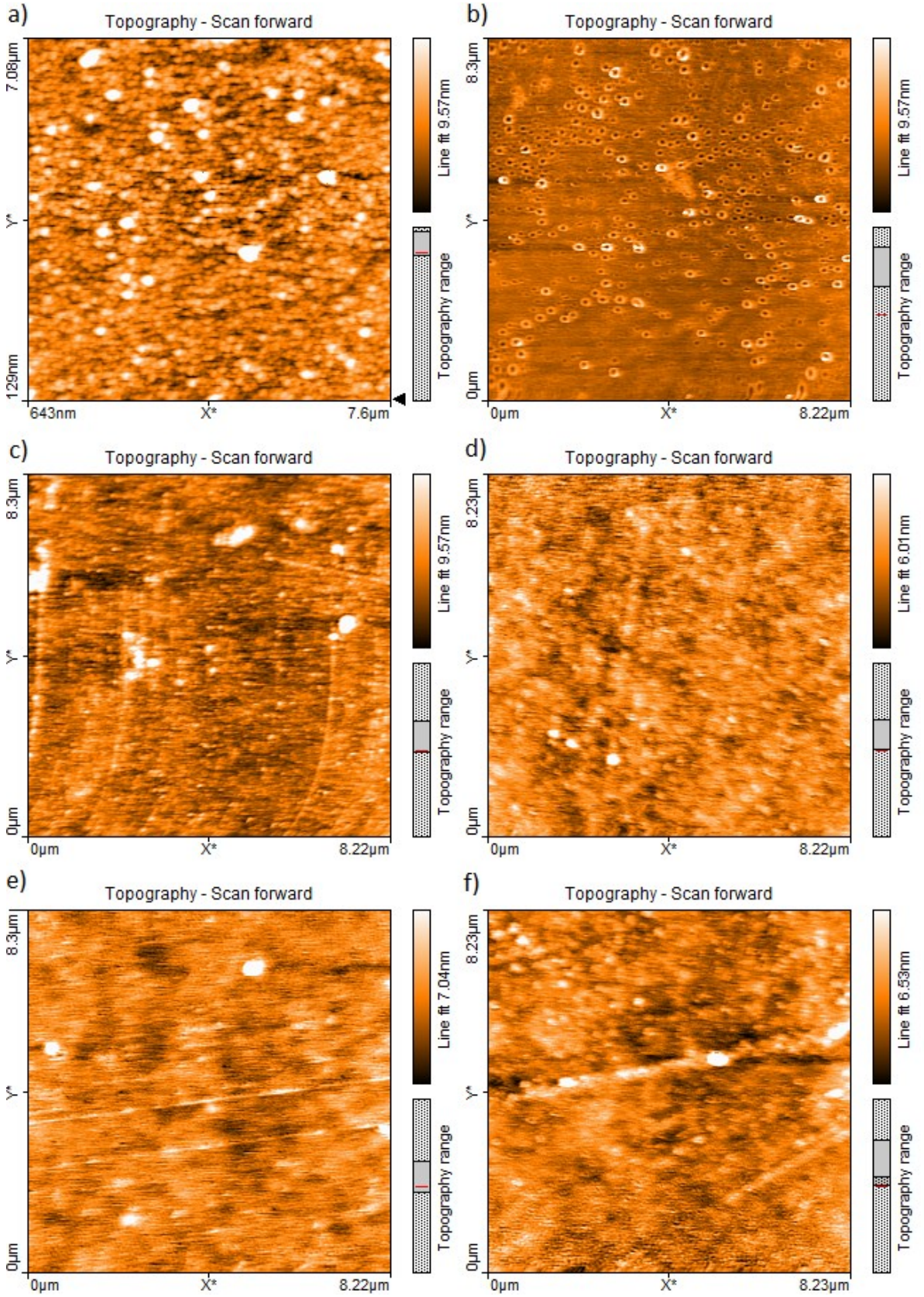

Figure 28: AFM results corresponding to a) the thermally annealed substrate, b) sample 1, c) sample 2, d) sample 3, e) sample 4 and f) sample 5.

4.6 Results for InN

Experiments for deposition on InN are summarized in Table 5. Samples 4,5,6 and 8 yielded no XRD peaks. From previous results of AlN this is indicative of the ITO layer being removed during deposition, but again there is no clear correlation between the plasma nitridation parameters and the disappearance of the ITO spectra. High power, low pressure nitridation steps were employed in samples 22 and 23. Both samples show the ITO spectrum has not been etched by the plasma, even though these present the best conditions for the high ion energy plasma etching within the parameters explored.

InN was found to be the only compound to have both the underlying annealed ITO spectrum and the (002) peak of a III-Nitride. Samples 1,2,3,7,22 and 23 were found to have both the expected ITO spectrum with the (002) peak of InN also clearly present. The FWHM and height of the peaks present in all samples can be seen in fig. 29 to be close to one another, with samples 3 and 22 being marginally greater in height than the rest. Fig. 29 also shows samples 2 and 23 having peaks corresponding to indium metal on the surface.

Samples 18, 20 and 21 were found to have the ITO spectrum present with no indication of InN present on the XRD results. Sample 18 only showed the presence of the ITO spectrum, while 20 and 21 show the ITO spectra with large metal peaks present. Indium metal can be seen in samples 2, 23, 21, 20 with the peaks increasing in that order. This corresponds to a decrease in the deposition pressure while keeping the vapour lines pressure constant.

Samples 9-17 and 19 show only peaks characteristic of InN without the presence of the ITO spectrum. Of these samples, numbers 9, 13 and 14 can be used to demonstrate the range of spectra observed (see fig. 31). From sample 14 in fig. 31 the onset of crystallization can be seen

to start with the appearance of the (002) peak of InN at approximately 31.6°. The position of this peak was common to all structures containing this peak, regardless of the presence of the ITO spectrum. Sample 13 shows the presence of the (102) peak around 43.6° and the (103) peak at 57°. The (103) peak was shown to have the greatest increase in height between samples, possibly indicating growth along this direction.

le 5: Summary of InN growth parameters.

ple	Temp (°C)	RPM	Cycles	Nitridation Time (s)	Power (W)	Nitridation pressure ratio	MO timing ratio	Deposition pressure ratio	Plasma Power (W)
	540	60	400	60	100	2.00	1	2.00	600
	540	60	600	60	100	2.00	1	2.00	600
	480	60	600	60	100	2.00	1	2.00	600
	540	60	400	60	100	1.33	1	1.00	500
	540	60	400	60	100	1.33	1	1.00	500
	540	60	400	60	100	1.33	1	1.00	600
	540	60	400	60	100	5.33	1	4.00	600
	540	60	400	60	100	5.33	1	2.00	600
	540	60	400	60	100	2.67	1	4.00	600
	540	60	400	60	100	1.60	1	4.00	600
	540	60	400	60	100	4.00	1	4.00	600
	540	60	400	60	100	2.00	1	3.00	600
	540	60	400	60	100	3.33	1	2.50	600
	540	60	400	60	100	5.33	1	2.67	600
	540	60	400	60	100	5.33	1	3.20	600
	540	60	400	60	100	5.33	1	5.33	600
	460	60	400	60	100	5.33	1	5.33	600
	460	60	400	60	300	14.29	0.5	14.29	300
	460	60	400	60	200	10.00	0.5	10.00	200
	460	60	400	60	200	10.00	1	10.00	200
	460	60	400	60	200	10.00	0.8	10.00	200
	460	60	400	60	600	3.33	0.8	3.33	600
	460	60	400	60	400	5.00	0.8	5.00	200

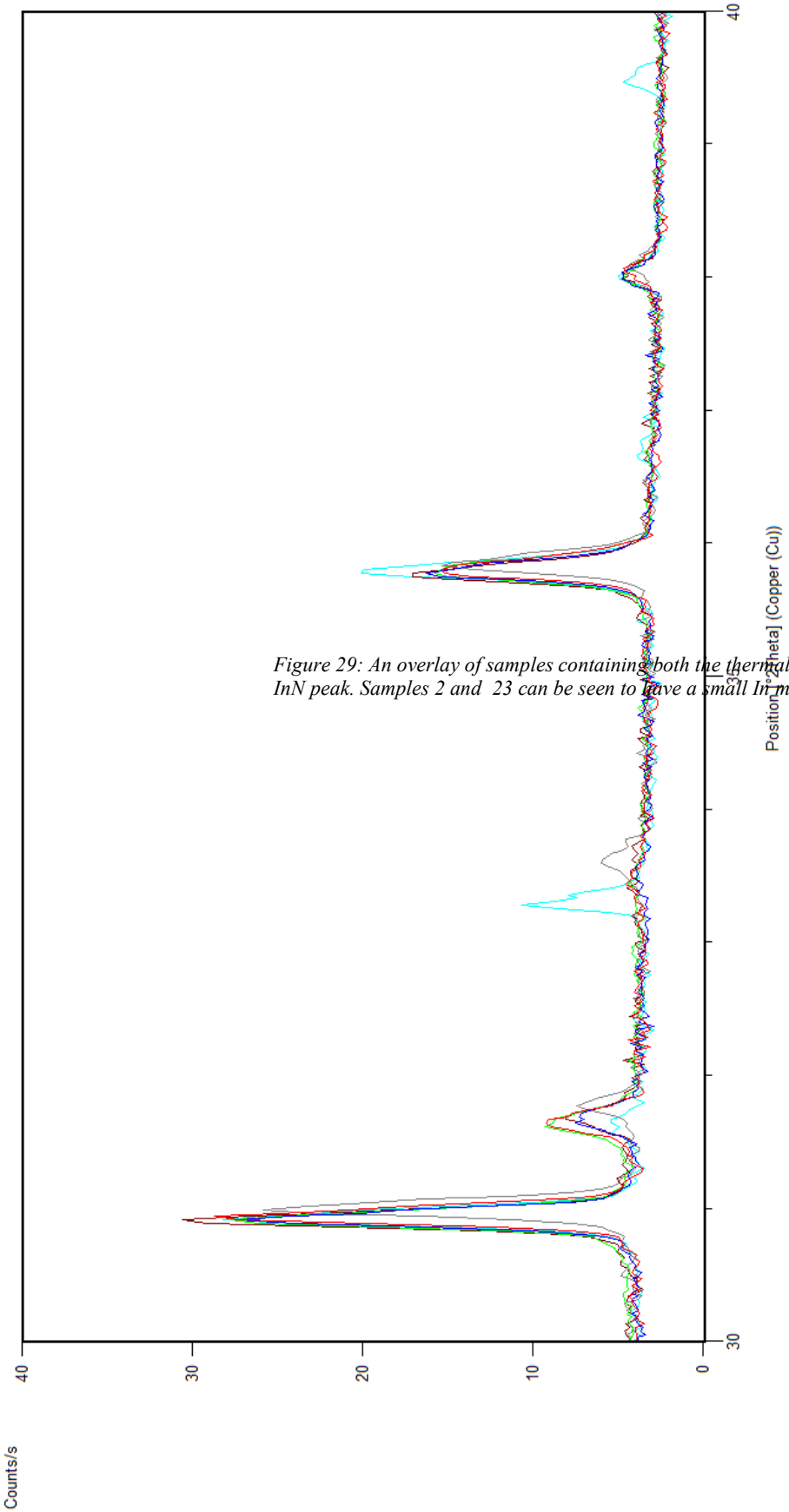

Figure 29: An overlay of samples containing both the thermally annealed ITO spectrum and the (002) spectrum of In InN peak. Samples 2 and 23 can be seen to have a small In metal peak.

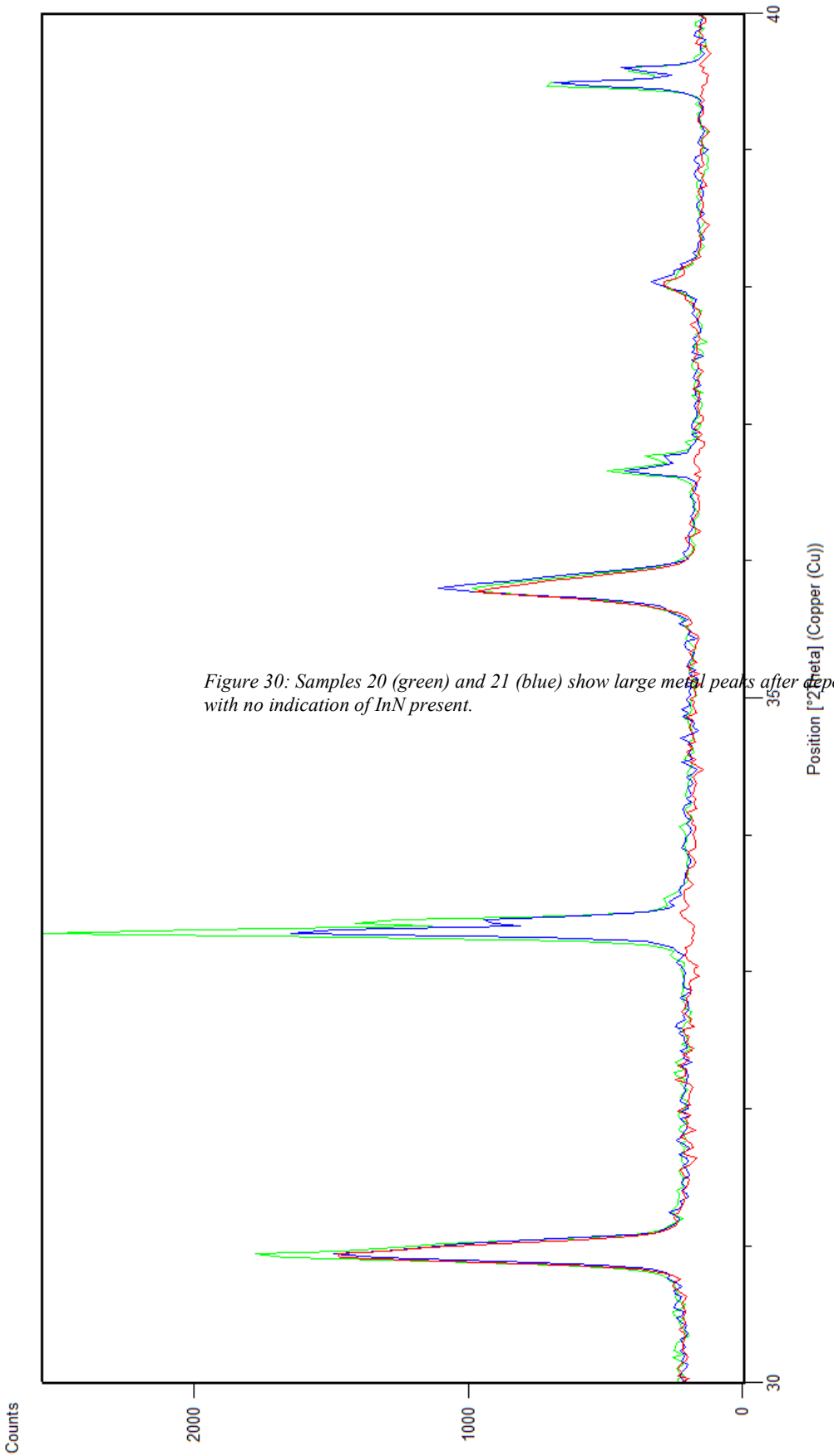

Figure 30: Samples 20 (green) and 21 (blue) show large metal peaks after deposition with a lack of the (002) peak. Sample 1
with no indication of InN present.

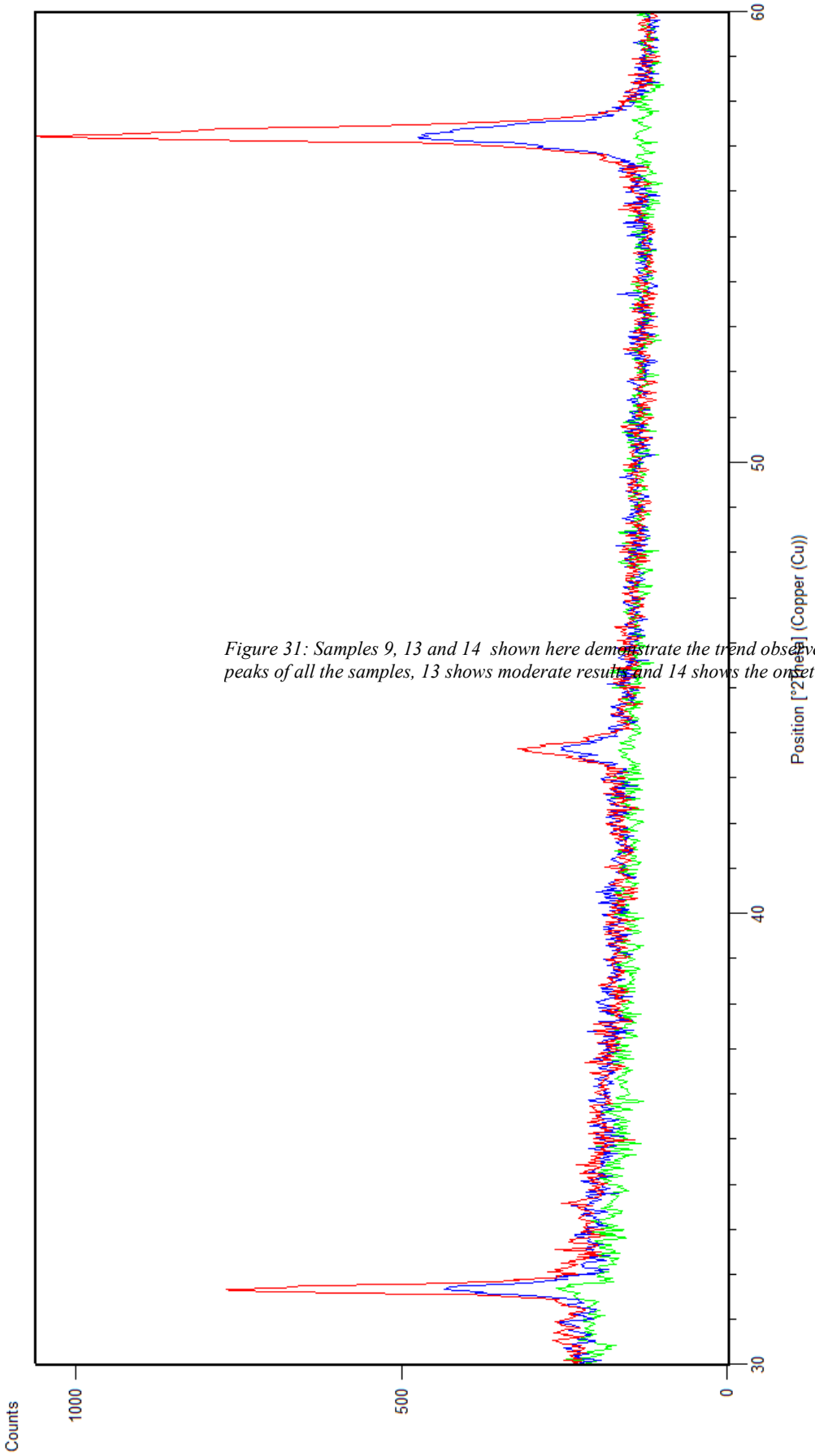

Figure 31: Samples 9, 13 and 14 shown here demonstrate the trend observed in XRD peaks of InN observed without the A peaks of all the samples, 13 shows moderate results and 14 shows the onset of the (002) peak with no other peaks present

Comparison of samples 3 and 9 were done under the SEM to investigate differences between samples containing InN XRD peaks with the ITO spectra as in fig. 32 (sample 3) and without, as in fig. 31 (sample 9). Sample 3 SEM results can be seen in fig. 32 and sample 9 in fig. 33. Both samples show a similar thickness, assuming that the ITO thickness was the same in both cases. Sample 3 therefore shows a slower growth rate than samples 9 despite the timing of the metal-organic being the same, since 200 more cycles were used in sample 3. The differences between growth sample 3 and 9 was the nitridation pressure being lowered, the temperature was increased from 480 to 540°C and the vapour line pressure was increased. From the increase in temperature a higher growth rate can be expected but was not observed. This indicates the relative pressure of the vapour line and chamber has an effect on the growth rate.

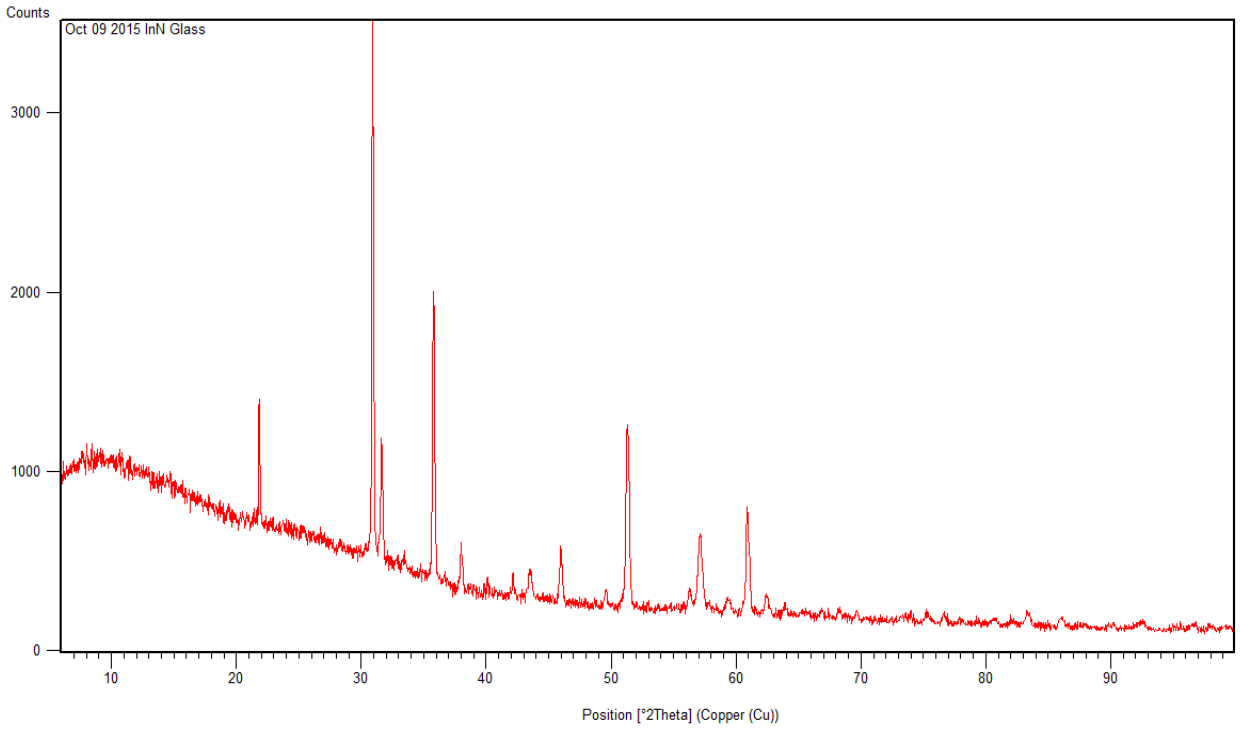

Figure 32: XRD results of sample 3.

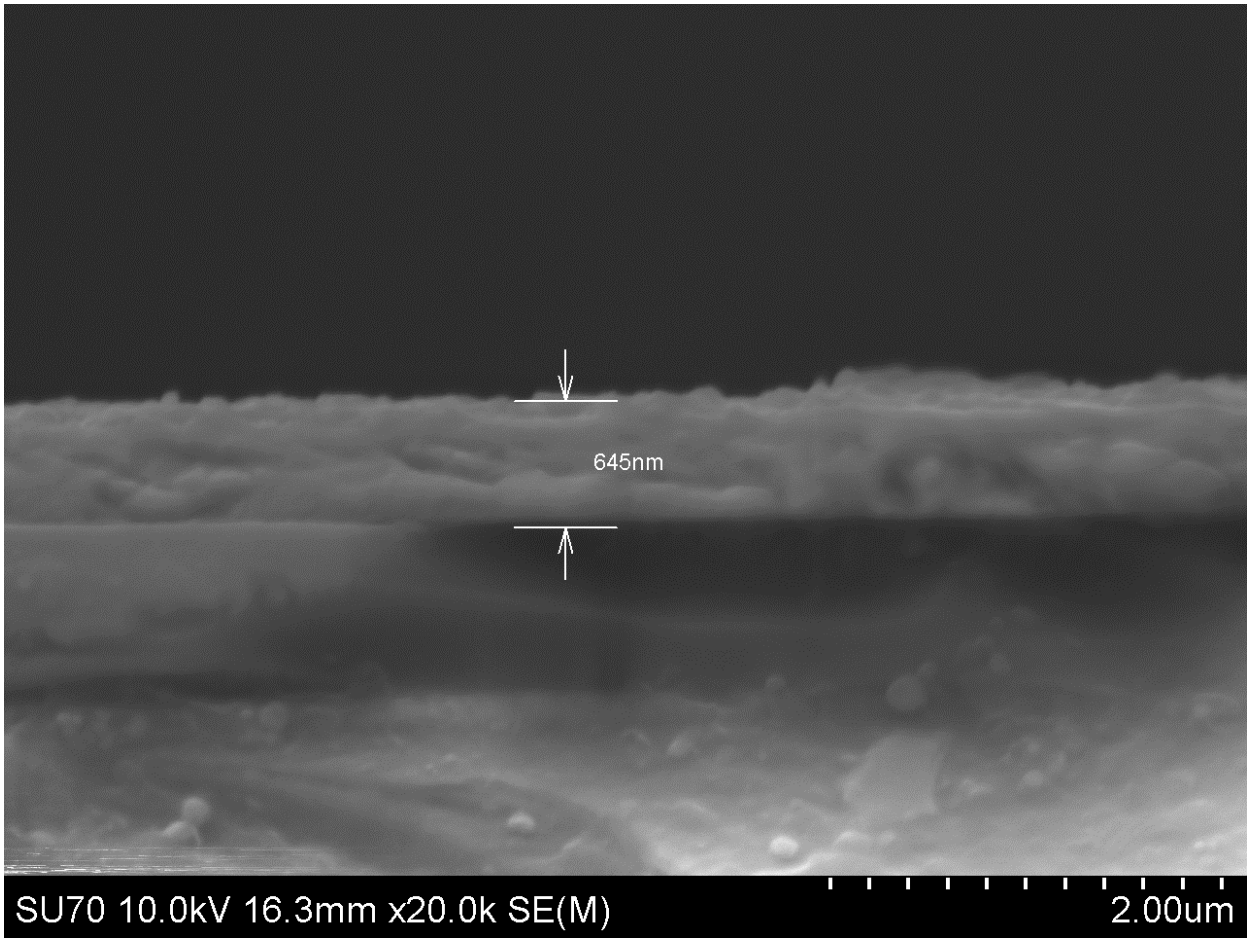

Figure 33: SEM cross section of sample 3. XRD results of this sample show the underlying ITO has been annealed and the presence of (002) InN can be seen.

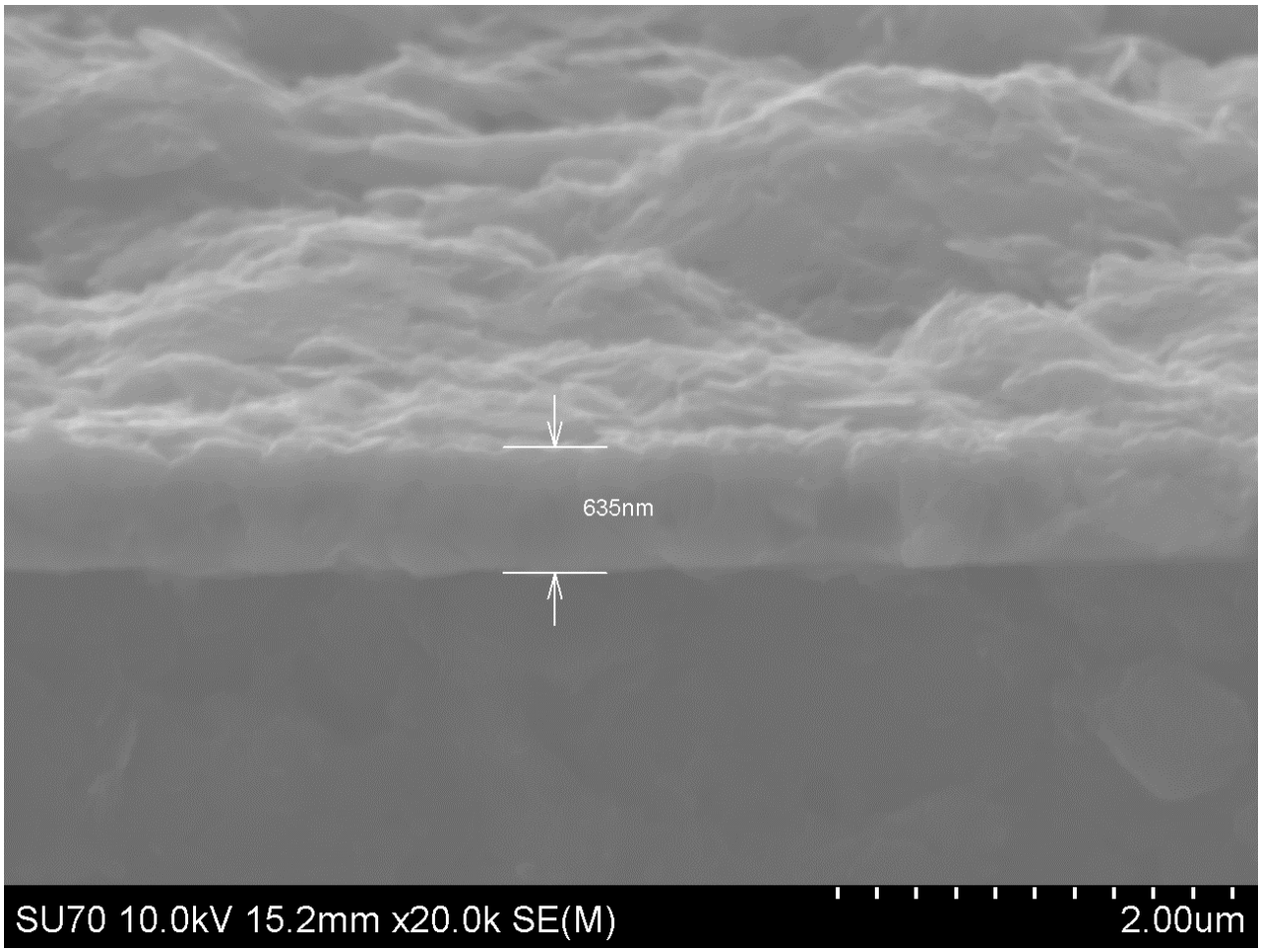

Figure 34: SEM cross section of sample 9. XRD results of this sample show no ITO spectrum has been annealed and the presence of (002) InN can be seen.

SEM results for sample 17 can be seen in fig. 35. Sample 17 showed the same peaks present as sample 9 in the XRD spectrum (fig. 36), but at a lower height for the same number of deposition cycles and demonstrates a significantly thinner layer. The differences from sample 9 to 17 were the growth temperature was lowered from 540°C to 460°C, the vapour line pressure was increased and the chamber pressure was increased. The thinner layer corresponding to higher pressures in the vapour line contrasts with results from samples 3 and 9 previously discussed.

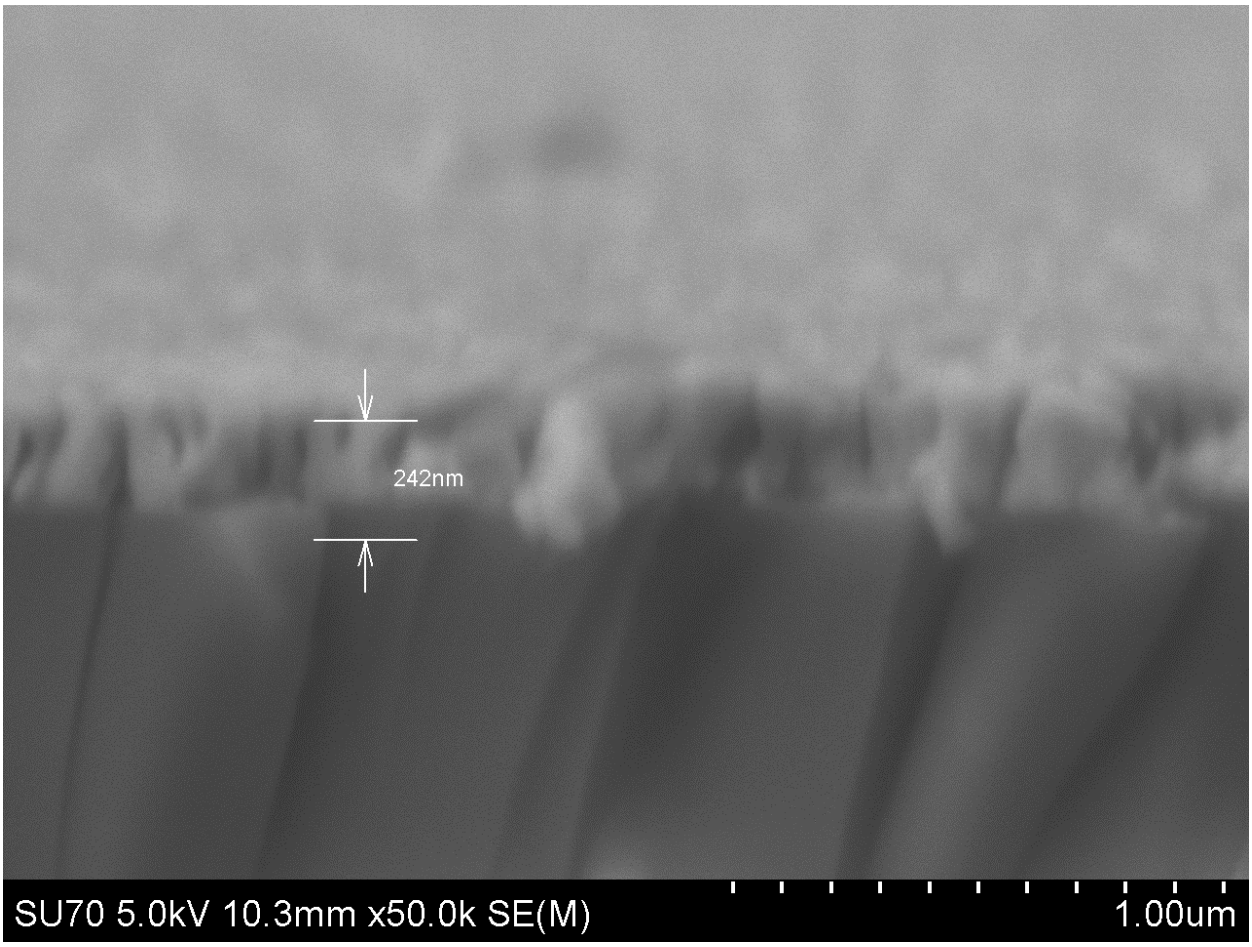

Figure 35: SEM image of sample 17 showing a thickness of approximately 242nm.

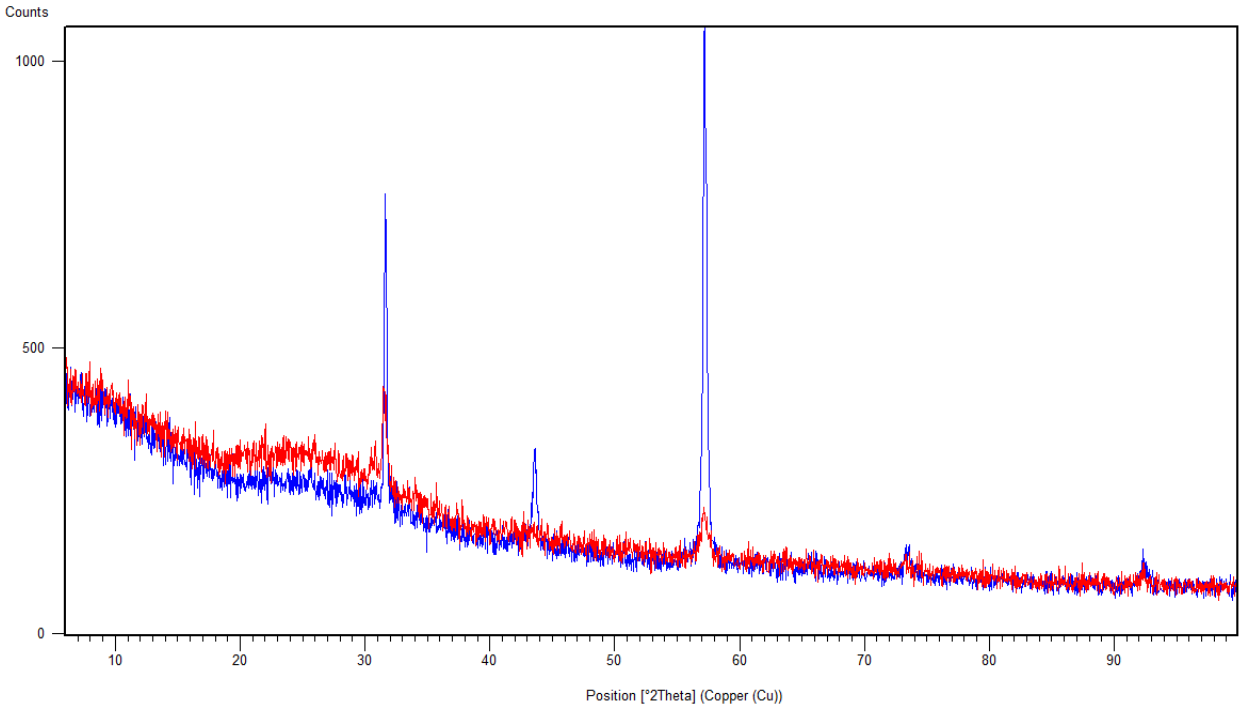

Figure 36: A comparison of samples 9 and 17. The higher peaks belong to sample 9.

Optical absorption data gathered from the spectrophotometer can be seen in fig. 37. From the shape of the absorption edge, samples 9 and 10 show similar optical quality. The XRD results of these samples are near identical as well. The difference between growth 9 and 10 was a decrease in vapour line pressure and a decrease in growth pressure. These results demonstrate that this had next to no effect on the sample quality. Samples 9 and 10 had the sample growth temperature as samples 1, 2, 3 and 16. They also demonstrate a common set of XRD peaks with 16 but with higher peak values. The difference between samples 16 and 17 was a decrease in the temperature from 540°C to 460°C. This to a slight decrease in the metal peaks present, indicating indium desorption may be occurring.

Samples 1, 2 and 3 all show curves similar to those seen in fig. 24 for AlN and fig. 27 for GaN, although EDX measurements of sample 3 and XRD results show ITO and InN are present.

Since this curve is similar to AlN results showing no In in EDX results, this is possibly due too the glass substrate used.

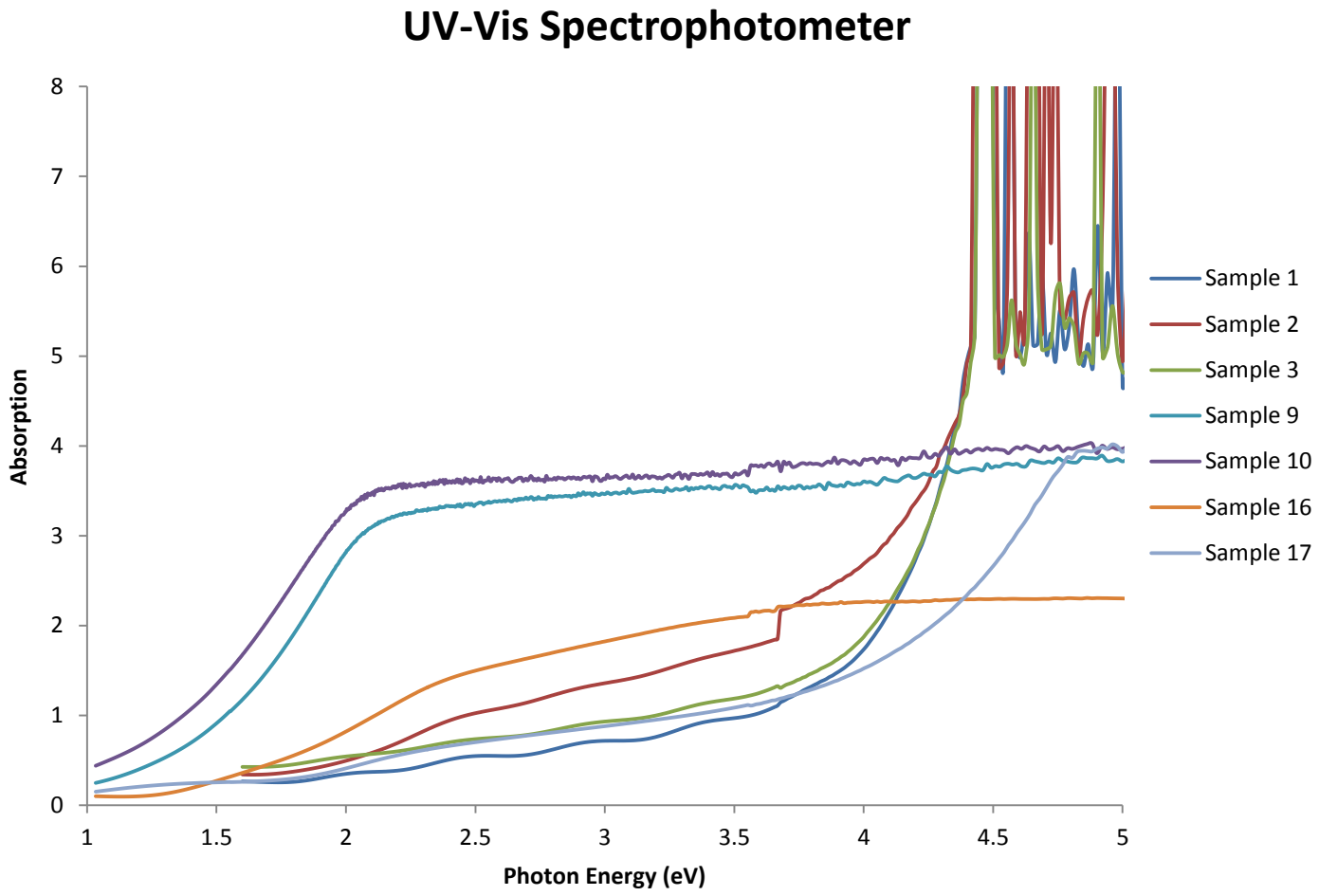

Figure 37: UV-Vis Spectrophotometer data gathered for 7 samples. Samples 9 and 10 can be seen to have the best absorption curves with absorption edges below 1.5eV.

Overall the best results for InN were obtained from sample 9 for growths without the ITO spectrum and sample 22 for growths with the ITO spectrum. An overlay of their XRD spectra can be seen in fig. 38. It can be seen that even though the growth length for both samples was the same, sample 9 showed a greater rate of crystallinity, especially at the (103) peak, even without the ITO spectrum seen.

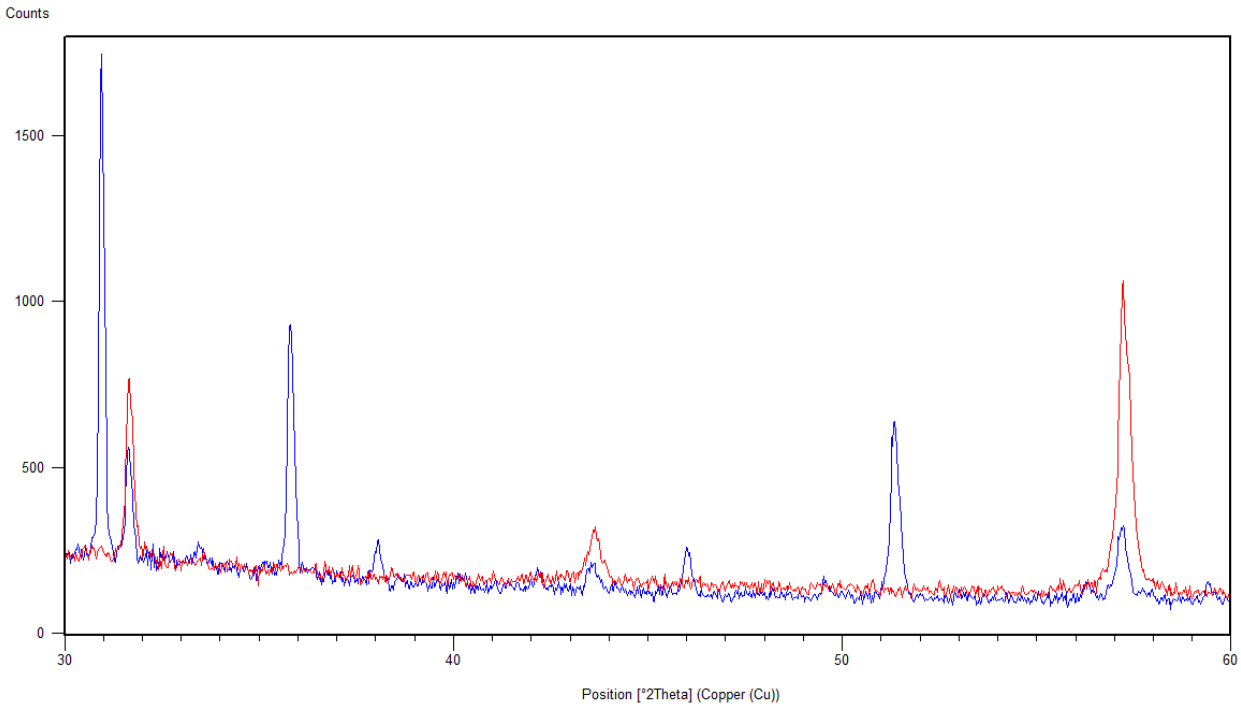

Figure 38: Samples 9 and 22, representing the best results for the case of the ITO spectrum being seen (sample 22) and it disappearing (sample 9).

Chapter 5: Band Structure Calculations

5.1 Overview

This section contains a theoretical investigation in the electronic band structure of InN and the influence of non-stoichiometric nitrogen, carbon substitution and interstitial oxygen on the band gap of the resulting structures.

5.2 Electron Band Structure of a Generic Crystal AxB1-xC

The electronic band structure of the multinary $A_xB_{1-x}C$ crystal considers large primitive supercells which satisfy certain conditions of spatial periodicity to be comprised of smaller elementary cells. The electronic band structure of the crystal can be determined by electron interactions within primitive supercell. The mathematical formalism behind this has been developed elsewhere [52]. The important concept is that the electron band structure of the multinary cell contains the same sub bands as the supercell without localization interactions, which is comprised of a sum of its constituent elementary cell band structures. Each elementary cell also has symmetry equal to the primitive cell of crystals comprised of AC and BC if the positions of the cations and anions have no consideration for the nature of the atoms. For binary crystals the elementary cell would therefore be equal to the primitive cell.

For the purposes of determining the role of carbon substitution in InN, these quasi elementary cells are with a composition of InC_yN_{1-y}. Each of the primitive cells is created by varying the y parameter is varied from 0 to 1 over five elementary cells, beginning with pure InC and replacing anionic carbon with nitrogen until pure InN is reached.

For determining the role of non-stoichiometric nitrogen in InN, the quasi elementary cells are comprised of nitrogen on the cationic site and indium on the anionc site. Each of the supercell is

created by replacing an anionic indium with nitrogen. This varies the composition from pure InN to pure N-N over five elementary cells.

5.2 Optical Phenomena

The optical properties of disordered semiconductors are investigated in [52]. There are two main types:

i. Tunnel optical absorption

This phenomenon arises from the overlapping of electron states in the conduction and valence band of different elementary cells. Despite the fact that an energy barrier may exist for the electron in the valence band, it may tunnel directly into the conduction band. The energy of the transition is the difference of the original valence band and the transition conduction band.

ii. Exciton Attraction

Coulomb forces existing between electrons in the conduction band pocket of an elementary cell and a valence band hole of another cell form a quasi-particle characterized by a binding energy and hydrogen like energy levels.

5.3 Interstitial Oxygen Impurity States

Oxygen is a common contaminant in MOCVD. The impurity has two possible roles in the lattice. It can substitute on nitrogen sites to form a ternary compound of InNO or it can become an isolated as an interstitial atom in the lattice. The oxygen atom may be considered non-isolated if impurity levels are high enough that spatial coupling with other interstitials

occurs, but this is not considered. The hydrogen like isolated orbitals of impurity O atoms is investigated for following cases:

i. Incorporation of the oxygen atom in a cluster of pure InC_yN_{1-y}

ii. Incorporation of the oxygen atom in cluster of non-stoichiometric InN:N

5.4 Electron Band Structures of InCyN1-y and of Non-Stoichiometric InN:N

LCAO electron band structures of both wurtzite InC_yN_{1-y} and non-stoichiometric InN:N for points Γ are calculated by the method given in [52]. The investigation shows that for the purpose of inter-band electron transitions for semiconductor compound alloys, parts of the LCAO electron band structure can be taken corresponding to the configurations of the quasi-elementary cells giving the best combination of deep energy pockets for the electrons in the conduction band, tallest energy pockets of holes in the valance band and the shortest distances between those pockets. To satisfy these three conditions five different types of wurtzite quasi-elementary cells are taken and labeled as follows:

1) InC quasi-elementary cell with 2 carbon atoms and 2 indium atoms corresponding go pure InC
2) InNC quasi-elementary cell with 1.5 carbon atoms, 0.5 nitrogen and 2 indium
3) InNC quasi-elementary cell with 1.0 carbon atoms, 1.0 nitrogen and 2 indium
4) InNC quasi-elementary cell with 0.5 carbon atoms, 1.5 nitrogen and 2 indium
5) InN quasi-elementary cell with 2 nitrogen atoms and 2 indium atoms corresponding go pure InN

For the analysis of non-stoichiometric InN:N

1) Pure N-N
2) InN:N quasi-elementary cell with 1.5 nitrogen atoms, 0.5 indium and 2 nitrogen
3) InN:N quasi-elementary cell with 1 nitrogen atom, 1 indium and 2 nitrogen
4) InN:N quasi-elementary cell with 0.5 carbon atoms, 1.5 indium and 2 nitrogen
5) InN quasi-elementary cell with 2 indium atoms and 2 nitrogen atoms

corresponding go pure InN

The LCAO electron band structure calculations for each quasi-elementary cell are performed by the method described in [52]. The electron energy terms ε_s and ε_p for both In atoms and N atoms are taken from [53].

MATLAB software has been used for all calculations. The calculated electron band structures are provided in fig. 39 for InC_yN_{1-y} and in fig. 40 for non-stoichiometric InN:N. The energy levels Γ_v^n and Γ_c^n are determined by taking the vacuum energy level as zero. The energy difference $\Gamma_c^n - \Gamma_v^n$ gives the band gap of sector n.

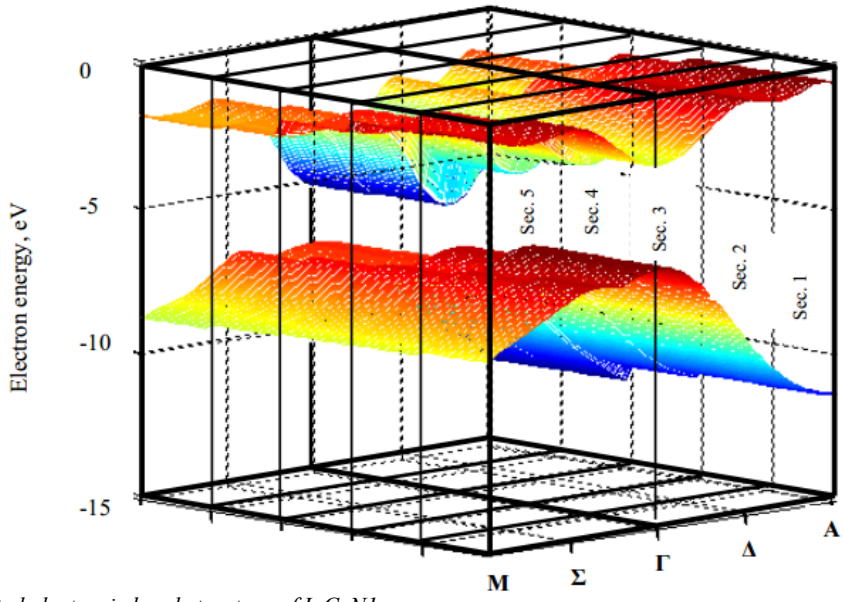

Figure 39: Calculated electronic band structure of InCyN1-y.

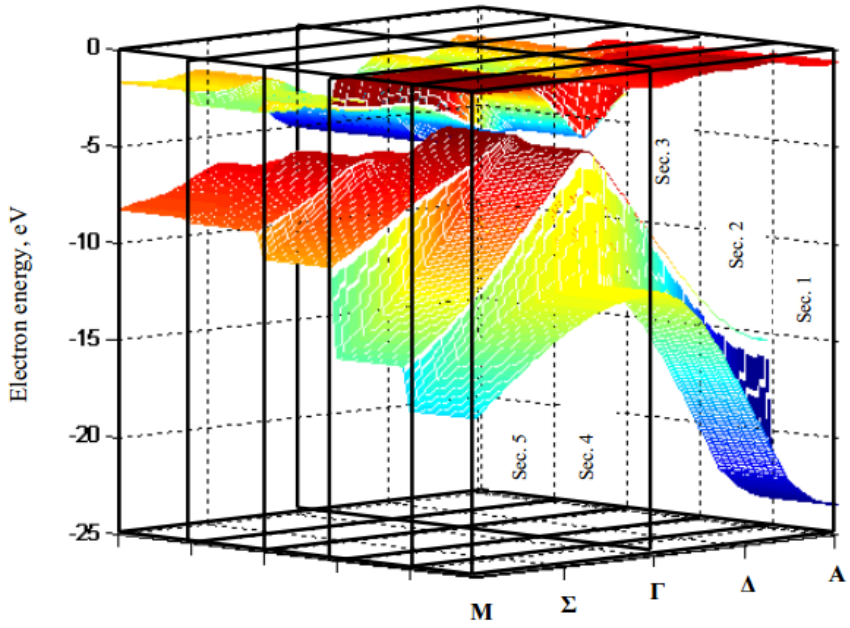

Figure 40: Calculated electronic band structure of non-stoichiometric InN:N.

The corresponding band diagrams at the Γ point for each primitive cell can be seen in fig. 41 and fig. 42.

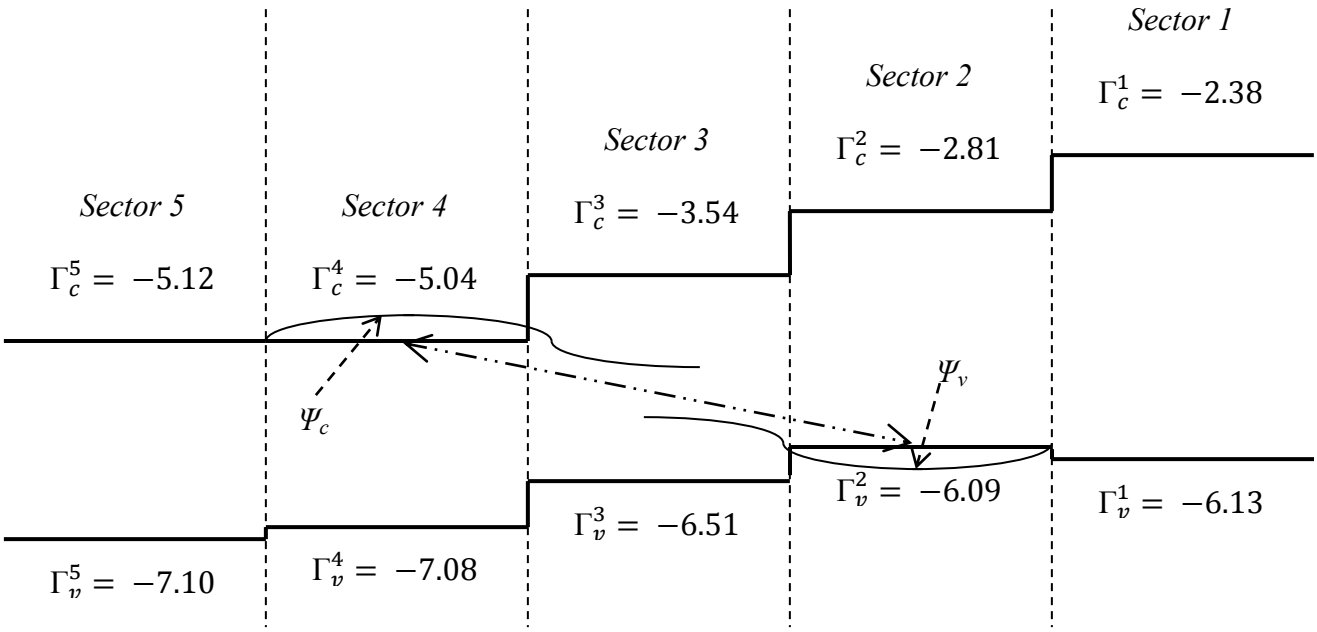

Figure 41: Electron band diagram of InCyN1-y for point Γ.

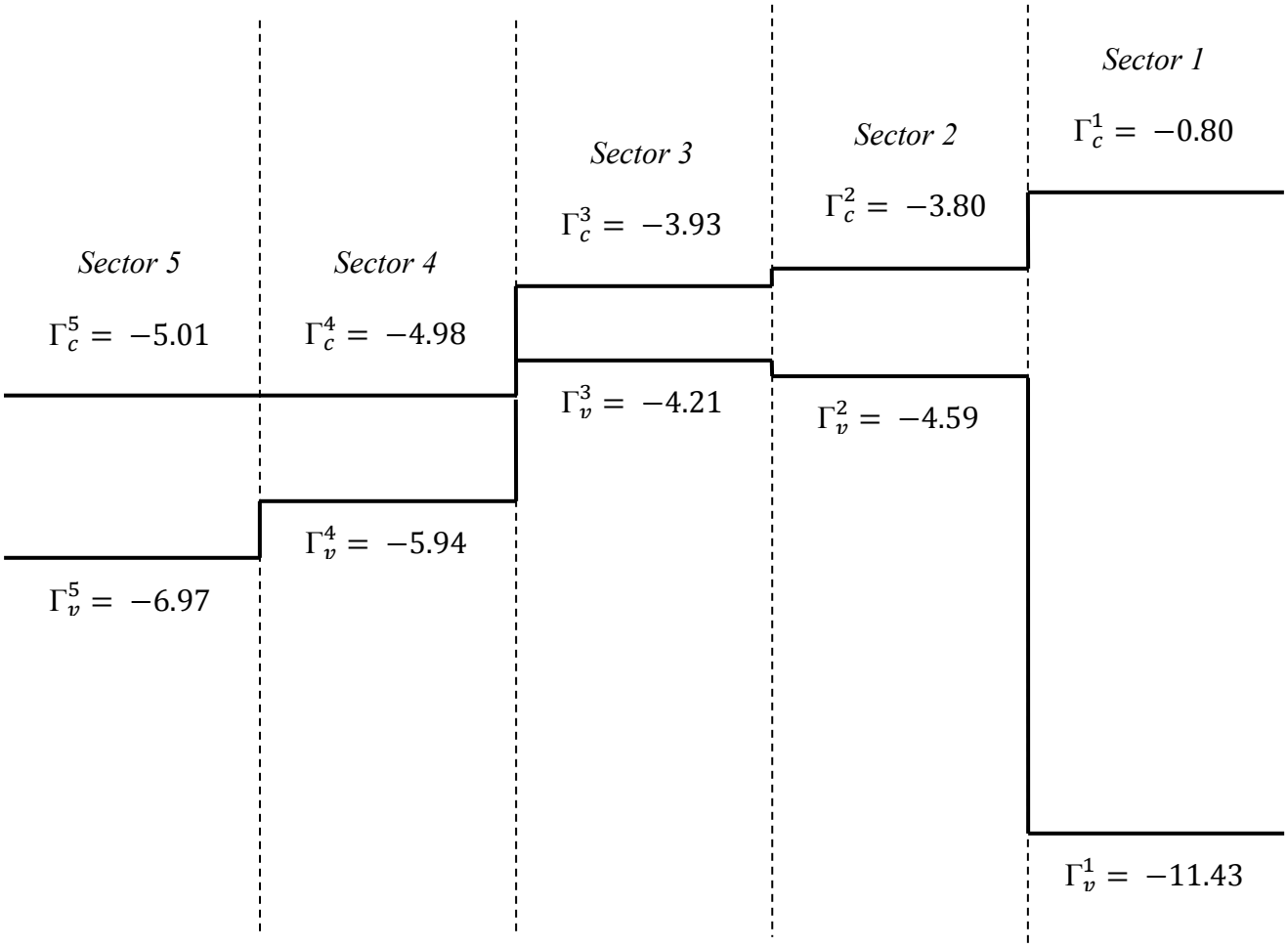

Figure 42: Electron band diagram of non-stoichiometric InN:N for point Γ.

Several important features of the calculated band structures can be seen in figs. 39-42. In fig. 39 two pockets of similar energy can be seen in the conduction band over all compositions. This would indicate the possible presence of holes in the valence band with two different effective masses, leading to holes with different levels of mobility within the structure.

In fig. 41 the tunnel optical absorption between Γ_v^2 and Γ_c^4 is shown with a corresponding tunnel optical absorption edge of 1.05 eV. This indicates that carbon contamination may have been a source of the long standing confusion around the optical band gap of InN which was attributed to poor quality growth

In fig. 40 and 42 an overlap between Γ_v^3 and Γ_c^4 can be seen. This indicates that in the case of the primitive cell having two nitrogen has substitutions on indium sites; they may act as donors for single substations of nitrogen and pure InN. The three dimensional plot in fig.40 also reveals that at high levels of non-stoichiometry of nitrogen (sectors 2, 3 and 1) the hole mobility increases.

5.5 Electronic Structures of Isolated Oxygen Impurity States

The electronic structure of isolated oxygen impurity states were determined by considering that the valence electrons of an incorporated interstitial atom are not engaged in forming of ion-covalent bonds

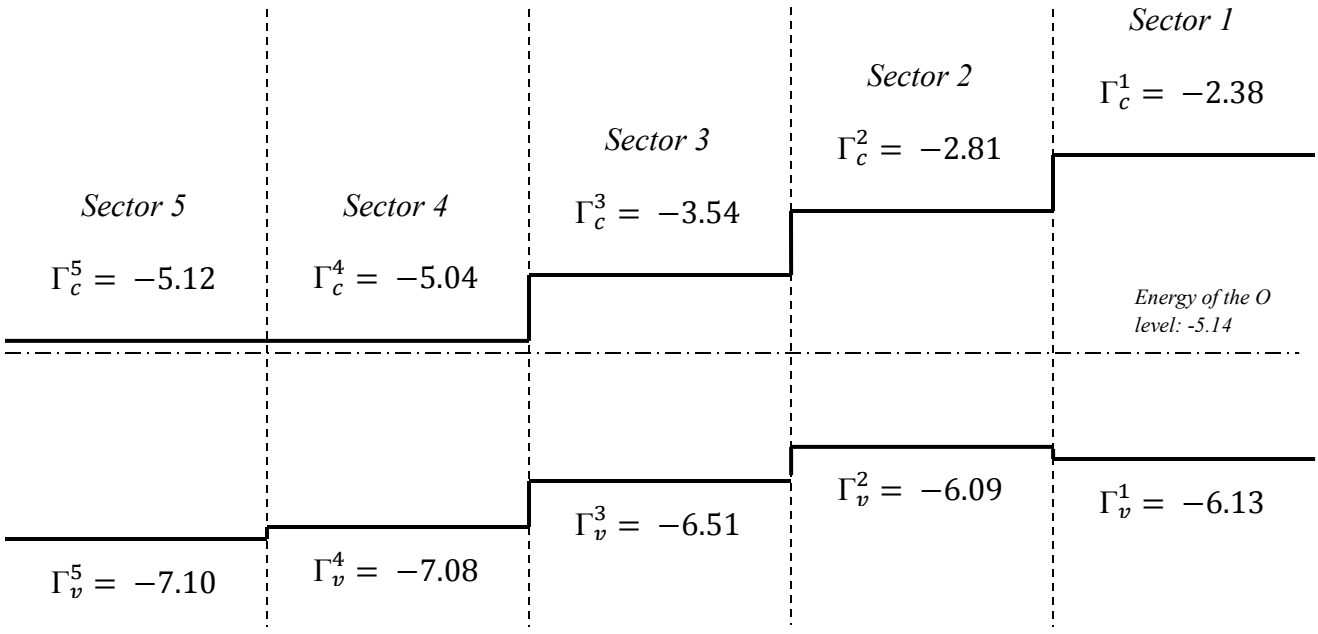

Figure 43: Electron band diagram of InCyN1-y for point Γ with the energy level of O impurity that is interstitially incorporated in InN primitive cell.

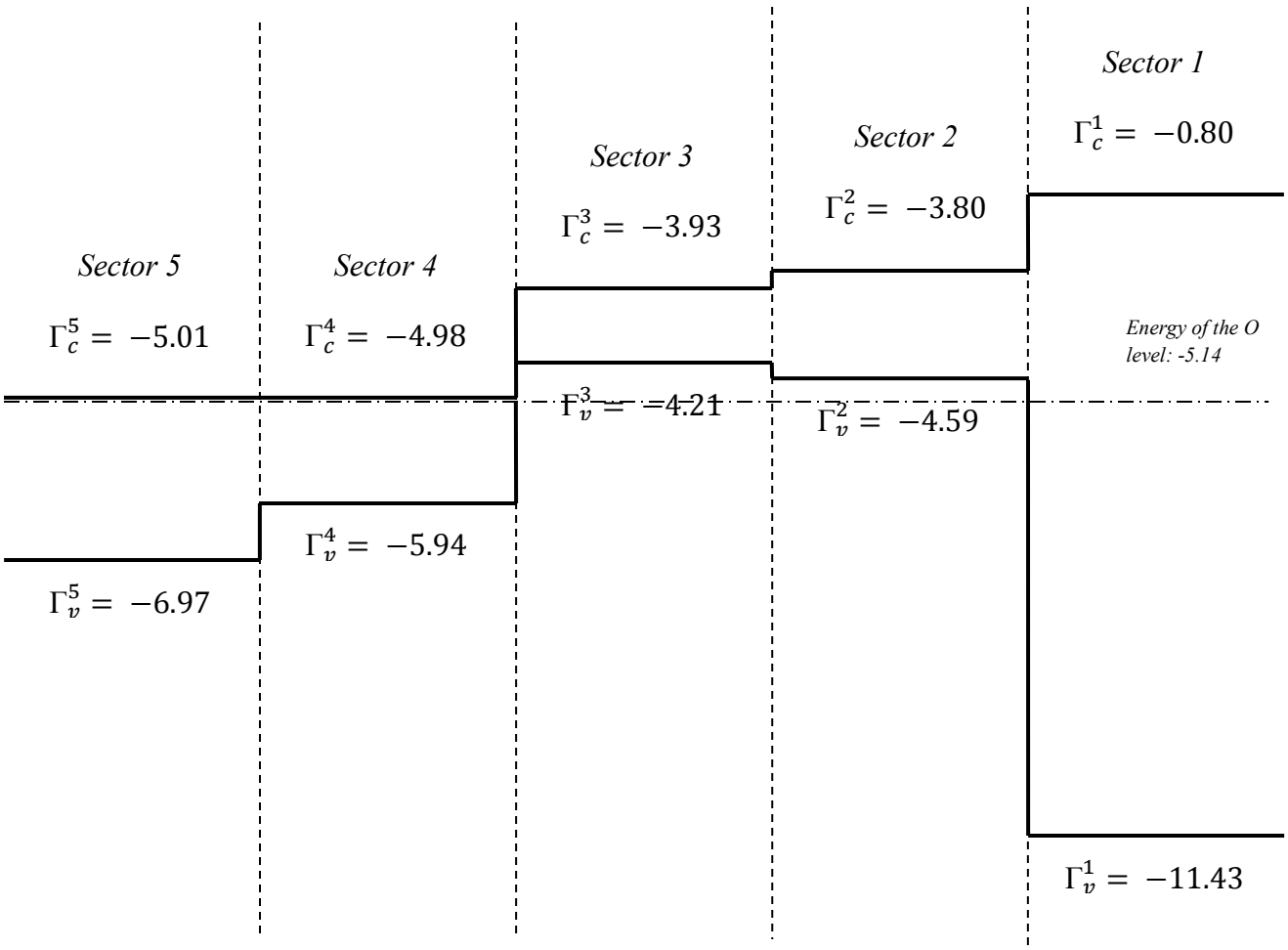

Figure 44: Electron band diagram of InN:N for point Γ with the energy level of O impurity that is interstitially incorporated in InN primitive cell.

A hydrogen like impurity analysis was performed under the assumption of long distance influence of the valence states from the oxygen atom. The Schrödinger equation for a hydrogen atom can therefore be used, but with effective masses and dielectric constants from the quasi primitive cells. The Schrödinger can be written as

$$\left(\frac{-\hbar\nabla^2}{2m} - \frac{e^2}{\kappa r}\right) F(r) = EF(r)$$

Where e is the electron charge, κ is the dielectric constant of the primitive cell and m is the electron effective mass. $F(r)$ is the ground state wave function of the form

$$F(r) = (\pi a^3)^{-1/2} e^{-r/a}$$

Where a is the effective Bohr radius that determines the localization radius of the wave function. This can be determined by

$$a = \frac{\hbar^2 \kappa}{me^2}$$

The solution the Schrödinger equation under these conditions gives energy levels described by

$$E_n = \frac{-e^4 m}{2n^2 \kappa^2 \hbar^2}$$

Where n is a non-zero integer. For the determination of isolated electron states n is taken as 1. From this treatment of the oxygen atoms, it can be seen that in fig. 43 it acts as a shallow donor in sectors 4 and 5, with increasing activation energy as the amount of carbon increases. From fig. 44 it can again be seen in sectors 4 and 5 it acts as a shallow donor, but as the amount of non-stoichiometric nitrogen is increased in sectors 3 and 2, the oxygen energy level can be seen to be inside the valence band. This indicates that it freely donates an electron to the valence band. In the case of pure nitrogen is a deep donor level.

Chapter 6: Conclusions and Future Work

The growth of III-nitrides utilizing low temperature techniques has been demonstrated and analyzed. The ITO glass system has proven to be a possible candidate for very large area nitride devices in the future.

Attempts at the deposition of GaN have resulted in amorphous GaN layers, verified by SEM measurements. Though no crystallinity was observed, the total thickness of GaN could be seen under the SEM to be consistent with other growths. Similar cases were observed in AlN and InN.

Deposition of AlN has resulted in mostly amorphous AlN. Utilzing the result from InN, one sample has shown promise with an InAlN grading layer. The InAlN system has not been a subject of analysis using this reactor and the growth of ternary compounds is outside the scope of this work. Graded buffer structures from InN to AlN and GaN are possible subjects of future work.

InN has proven to be the most successful candidate for epitaxy on ITO glass. The presence and variation of the (002) peak is promising for device application. SEM measurements confirm the presence of crystalline InN on ITO interlayers.

Theoretical calculations using LCAO has shown the possibility of carbon contamination as a source of optical absorption phenomena in the 1.04eV range. Second and triple order non-stoichiometric nitrogen in InN has been shown to result in the overlap of valence energy levels with conduction energy levels in lower substitutions. These results may be useful in explaining high levels of donor dopants in N rich growth.

The position of oxygen in the band structure of InN has shown it can act as a shallow donor in pure InN, and single substitution carbon impurities on nitrogen sites. This behavior was shown to extend to a single substitution of nitrogen in an indium site in non-stoichiometric InN. In higher levels of nitrogen substitution it was shown to act as a valence band donor.

Further optimization of growth conditions would likely focus on the plasma parameters available as well as its composition. In the growth techniques examined, plasma pressure was constantly held at the same pressure as the metal-organics. This may be changed during the growth cycle to vary the composition of nitrogen reaching the substrate. The use of entirely nitrogen plasma could also be changed to a hydrogen-nitrogen plasma mixture to explore plasma assisted adatom migration.

Future work in device development has many possibilities. For InN, sensor devices such as the ion selective field effect transistors can be fabricated with only a single layer and device contacts. These could be immediately fabricated and characterized. Because of the uniquely high difference in hole and electron mobility, InN also has potential research opportunities as a THz radiation source utilizing the photo-dember effect.

Further development of crystalline single layers of AlN and GaN could lead to their application in schottky based sensors. The wide band gap of these materials also allows them to act as hole blocking layers if additional device layers are deposited. A potential application of this is with amorphous selenium based x-ray detectors. AlN and GaN may also lead to the development of ternary layers. This can allow the design and fabrication of double heterojunction structures utilizing only equipment found at Lakehead University.

[1] J. Wu, W. Walukiewicz, W. Shan, K. M. Yu, J. W. A. Iii, S. X. Li, E. E. Haller, H. Lu, and W. J. Schaff, "Temperature dependence of the fundamental band gap of InN," *J. Appl. Phys.*, vol. 94, no. 7, pp. 4457–4460, Oct. 2003.

[2] H. Morkoç and H. Morkoç, *Handbook of nitride semiconductors and devices*. Weinheim : [Chichester: Wiley-VCH ; John Wiley, distributor], 2008.

[3] E. F. Schubert, *Light-Emitting Diodes*. 2006.

[4] V. M. Polyakov and F. Schwierz, "Low-field electron mobility in wurtzite InN," *Appl. Phys. Lett.*, vol. 88, no. 3, p. 032101, Jan. 2006.

[5] S. K. O'Leary, B. E. Foutz, M. S. Shur, and L. F. Eastman, "Steady-State and Transient Electron Transport Within the III–V Nitride Semiconductors, GaN, AlN, and InN: A Review," *J. Mater. Sci. Mater. Electron.*, vol. 17, no. 2, pp. 87–126, Feb. 2006.

[6] C. J. Glassbrenner and G. A. Slack, "Thermal Conductivity of Silicon and Germanium from 300K to the Melting Point," *Phys. Rev.*, vol. 134, no. 4A, pp. A1058–A1069, May 1964.

[7] F. Bernardini, V. Fiorentini, and D. Vanderbilt, "Spontaneous polarization and piezoelectric constants of III-V nitrides," *Phys. Rev. B*, vol. 56, no. 16, pp. R10024–R10027, Oct. 1997.

[8] J. m. Phillips, M. e. Coltrin, M. h. Crawford, A. j. Fischer, M. r. Krames, R. Mueller-Mach, G. o. Mueller, Y. Ohno, L. e. s. Rohwer, J. a. Simmons, and J. y. Tsao, "Research challenges to ultra-efficient inorganic solid-state lighting," *Laser Photonics Rev.*, vol. 1, no. 4, pp. 307–333, Dec. 2007.

[9] C. Ronning, E. P. Carlson, and R. F. Davis, "Ion implantation into gallium nitride," *Phys. Rep.*, vol. 351, no. 5, pp. 349–385, Sep. 2001.

[10] C.-C. Yu, C. F. Chu, J. Y. Tsai, and S. C. Wang, "Investigation of beryllium implanted P-type GaN," *Mater. Sci. Eng. B*, vol. 82, no. 1–3, pp. 82–84, May 2001.

[11] S. C. Jain, M. Willander, J. Narayan, and R. V. Overstraeten, "III–nitrides: Growth, characterization, and properties," *J. Appl. Phys.*, vol. 87, no. 3, pp. 965–1006, Feb. 2000.

[12] G. B. Stringfellow, "Microstructures produced during the epitaxial growth of InGaN alloys," *J. Cryst. Growth*, vol. 312, no. 6, pp. 735–749, Mar. 2010.

[13] P. T. Barletta, E. A. Berkman, B. F. Moody, N. A. El-Masry, A. M. Emara, M. J. Reed, and S. M. Bedair, "Development of green, yellow, and amber light emitting diodes using InGaN multiple quantum well structures," *Appl. Phys. Lett.*, vol. 90, no. 15, p. 151109, Apr. 2007.

[14] A. G. Bhuiyan, A. Hashimoto, and A. Yamamoto, "Indium nitride (InN): a review on growth, characterization, and properties," *J. Appl. Phys.*, no. 5, 2003.

[15] S. State, *Crystal structure of ZnS (wurtzite) with coordination polyhedra*. 2008.

[16] H. Morikawa and M. Fujita, “Crystallization and electrical property change on the annealing of amorphous indium-oxide and indium-tin-oxide thin films,” *Thin Solid Films*, vol. 359, no. 1, pp. 61–67, Jan. 2000.

[17] Y.-S. Tang, S.-F. Hu, C. C. Lin, N. C. Bagkar, and R.-S. Liu, “Thermally stable luminescence of KSrPO4:Eu2+ phosphor for white light UV light-emitting diodes,” *Appl. Phys. Lett.*, vol. 90, no. 15, p. 151108, Apr. 2007.

[18] H. Amano, N. Sawaki, I. Akasaki, and Y. Toyoda, “Metalorganic vapor phase epitaxial growth of a high quality GaN film using an AlN buffer layer,” *Appl. Phys. Lett.*, vol. 48, no. 5, pp. 353–355, Feb. 1986.

[19] V. Pishchik, L. A. Lytvynov, and E. R. Dobrovinskaya, *Sapphire*. Boston, MA: Springer US, 2009.

[20] D. Doppalapudi, E. Iliopoulos, S. N. Basu, and T. D. Moustakas, “Epitaxial growth of gallium nitride thin films on A-plane sapphire by molecular beam epitaxy,” *J. Appl. Phys.*, vol. 85, no. 7, pp. 3582–3589, 1999.

[21] N. Onojima, J. Suda, and H. Matsunami, “Lattice relaxation process of AlN growth on atomically flat 6H-SiC substrate in molecular beam epitaxy,” *J. Cryst. Growth*, vol. 237–239, Part 2, pp. 1012–1016, Apr. 2002.

[22] L. Liu and J. H. Edgar, “Substrates for gallium nitride epitaxy,” *Mater. Sci. Eng. R Rep.*, vol. 37, no. 3, pp. 61–127, Apr. 2002.

[23] P. G. Neudeck, “Silicon carbide technology,” *VLSI Handb.*, vol. 20061800, 2006.

[24] J.-J. Huang, H.-C. Kuo, and S.-C. Shen, *Nitride Semiconductor Light-Emitting Diodes (LEDs): Materials, Technologies and Applications*. Woodhead Publishing, 2014.

[25] B. Gil, *III-Nitride Semiconductors and Their Modern Devices*. OUP Oxford, 2013.

[26] U. Betz, M. Kharrazi Olsson, J. Marthy, M. F. Escolá, and F. Atamny, “Thin films engineering of indium tin oxide: Large area flat panel displays application,” *Surf. Coat. Technol.*, vol. 200, no. 20–21, pp. 5751–5759, May 2006.

[27] K. Zhang, F. Zhu, C. H. A. Huan, and A. T. S. Wee, “Indium tin oxide films prepared by radio frequency magnetron sputtering method at a low processing temperature,” *Thin Solid Films*, vol. 376, no. 1–2, pp. 255–263, Nov. 2000.

[28] T. C. Gorjanc, D. Leong, C. Py, and D. Roth, “Room temperature deposition of ITO using r.f. magnetron sputtering,” *Thin Solid Films*, vol. 413, no. 1–2, pp. 181–185, Jun. 2002.

[29] A. K. Varshneya, *Fundamentals of Inorganic Glasses*. Elsevier, 2013.

[30] J. H. Choi, H. Y. Ahn, Y. S. Lee, K. Park, T.-H. Kim, K. S. Cho, C. W. Baik, S. I. Kim, H. Yoo, E. H. Lee, B. L. Choi, S.-D. Kim, Y.-W. Kim, M. Kim, and S. Hwang, “GaN light-

emitting diodes on glass substrates with enhanced electroluminescence," *J. Mater. Chem.*, vol. 22, no. 43, pp. 22942–22948, Oct. 2012.

[31] J. Bian, L. Miao, F. Qin, D. Zhang, W. Liu, and H. Liu, "Low-temperature ECR-PEMOCVD deposition of high-quality crystalline gallium nitride films: A comparative study of intermediate layers for growth on amorphous glass substrates," *Mater. Sci. Semicond. Process.*, vol. 26, pp. 182–186, Oct. 2014.

[32] M. Hiroki, H. Asahi, H. Tampo, K. Asami, and S. Gonda, "Improved properties of polycrystalline GaN grown on silica glass substrate," *J. Cryst. Growth*, vol. 209, no. 2–3, pp. 387–391, Feb. 2000.

[33] A.-B. Zhi, F.-W. Qin, D. Zhang, J. Bian, B. Yu, Z.-F. Zhou, and X. Jiang, "Low-temperature growth of highly c-oriented InN films on glass substrates with ECR-PEMOCVD," *Vacuum*, vol. 86, no. 8, pp. 1102–1106, Feb. 2012.

[34] J. S. Yuan, G. H. Yu, C. M. Yang, and M. Y. Wang, "Deposition and Characterization of GaN Films on ITO Glass Substrates by PECVD," *Mater. Sci. Forum*, vol. 610–613, pp. 446–449, 2009.

[35] H. Kim, J. S. Horwitz, G. Kushto, A. Piqué, Z. H. Kafafi, C. M. Gilmore, and D. B. Chrisey, "Effect of film thickness on the properties of indium tin oxide thin films," *J. Appl. Phys.*, vol. 88, no. 10, p. 6021, 2000.

[36] T. Ashida, A. Miyamura, N. Oka, Y. Sato, T. Yagi, N. Taketoshi, T. Baba, and Y. Shigesato, "Thermal transport properties of polycrystalline tin-doped indium oxide films," *J. Appl. Phys.*, vol. 105, no. 7, pp. 073709–073713, Apr. 2009.

[37] Q. Sun and J. Han, "Nonpolar and semipolar GaN heteroepitaxy on sapphire for LED application," 2010, vol. 7617, pp. 761717–761717–14.

[38] S. Nakamura, M. Senoh, and T. Mukai, "Highly P-Typed Mg-Doped GaN Films Grown with GaN Buffer Layers," *Jpn. J. Appl. Phys.*, vol. 30, no. Part 2, No. 10A, pp. L1708–L1711, Oct. 1991.

[39] M. Yang, B. Yao, Y. H. Sohn, and R. D. Sisson, "Simulation of the ferritic nitriding process," *Int. Heat Treat. Surf. Eng.*, vol. 5, no. 3, pp. 122–126, 2011.

[40] J.-S. Paek, K.-K. Kim, J.-M. Lee, D.-J. Kim, M.-S. Yi, D. Y. Noh, H.-G. Kim, and S.-J. Park, "Nitridation of sapphire substrate and its effect on the growth of GaN layer at low temperature," *J. Cryst. Growth*, vol. 200, no. 1–2, pp. 55–62, Apr. 1999.

[41] Y. Tsukada, Y. Enatsu, S. Kubo, H. Ikeda, K. Kurihara, H. Matsumoto, S. Nagao, Y. Mikawa, and K. Fujito, "High-quality, 2-inch-diameter *m* -plane GaN substrates grown by hydride vapor phase epitaxy on acidic ammonothermal seeds," *Jpn. J. Appl. Phys.*, vol. 55, no. 5S, p. 05FC01, May 2016.

[42] N. P, *English: Concept Drawing of a Molecular Beam Epitaxy Growth chamber*. 2013.

[43] H. B. Profijt, S. E. Potts, M. C. M. Van de Sanden, and W. M. M. Kessels, "Plasma-assisted atomic layer deposition: Basics, opportunities, and challenges," *J. Vac. Sci. Technol. A*, vol. 29, no. 5, p. 050801, 2011.

[44] T. Nagata, M. Haemori, Y. Sakuma, T. Chikyow, J. Anzai, and T. Uehara, "Hydrogen effect on near-atmospheric nitrogen plasma assisted chemical vapor deposition of GaN film growth," *J. Appl. Phys.*, vol. 105, no. 6, pp. 066106–066109, Mar. 2009.

[45] E. Iliopoulos, A. Adikimenakis, E. Dimakis, K. Tsagaraki, G. Konstantinidis, and A. Georgakilas, "Active nitrogen species dependence on radiofrequency plasma source operating parameters and their role in GaN growth," *J. Cryst. Growth*, vol. 278, no. 1–4, pp. 426–430, May 2005.

[46] K. s. a. Butcher, Afifuddin, P. p.-T. Chen, and T. l. Tansley, "Studies of the Plasma Related Oxygen Contamination of Gallium Nitride Grown by Remote Plasma Enhanced Chemical Vapour Deposition," *Phys. Status Solidi C*, vol. 0, no. 1, pp. 156–160, Jan. 2003.

[47] "PANalytical - Bragg's law." [Online]. Available: http://www.panalytical.com/Technology-background/Braggs-law.htm. [Accessed: 30-Mar-2016].

[48] B. D. Cullity and S. R. Stock, *Elements of X-ray Diffraction*. Prentice Hall, 2001.

[49] "How an SEM works." [Online]. Available: http://www.nanoscience.com/products/sem/technology-overview/how-sem-works/. [Accessed: 30-Mar-2016].

[50] A. A. R. S. Marouf and others, "Characterization of Polymethyl Methacrylate and Silicon Photovoltaic Cells after Processing by Laser Direct Writing Technique," Sudan University of Science and Technology, 2015.

[51] G. Legeay and X. Castel, "A gradual annealing of amorphous sputtered indium tin oxide: Crystalline structure and electrical characteristics," *Thin Solid Films*, vol. 520, no. 11, pp. 4021–4025, Mar. 2012.

[52] D. Alexandrov, "Excitons of the structure in wurtzite InxGa1−xN and their properties," *J. Cryst. Growth*, vol. 246, no. 3–4, pp. 325–340, Dec. 2002.

[53] F. Herman and S. Skillman, *Atomic structure calculations*. Prentice-Hall, 1963.